Supplementary Information for:

Catalan solids from superionic nanoparticles

Tong Bian[1], Ivan Lobato[2], Ji Wang[1], Tara A. Nitka[3], Tzuf Shay Peled[1], Byeongdu Lee[4], Sandra Van Aert[2], Sara Bals[2], Lela Vuković[3], Thomas Altantzis[2]*, Petr Král[5]* & Rafal Klajn[1]*

[1]Department of Molecular Chemistry & Materials Science, Weizmann Institute of Science, Rehovot 76100, Israel
[2]Electron Microscopy for Materials Science (EMAT), University of Antwerp, Antwerp 2020, Belgium
[3]Department of Chemistry and Biochemistry, University of Texas, El Paso, TX 79966, USA
[4]X-Ray Science Division, Argonne National Laboratory, Argonne, IL 60439, USA
[5]Departments of Chemistry, Physics, and Biopharmaceutical Sciences, University of Illinois, Chicago, IL 60607, USA

*e-mail: rafal.klajn@weizmann.ac.il; pkral@uic.edu; thomas.altantzis@uantwerpen.be

Table of contents

1. Synthesis of charged nanoparticles

1.1. Colloidal synthesis of gold and palladium nanoparticles

- Size-uniform gold nanoparticles with sizes in the range 2.58–4.19 nm were synthesized by reducing $HAuCl_4$ with borane–*tert*-butylamine (BTBA) complex in toluene in the presence of oleylamine (OLA), by modifying a previously reported procedure[1]. The size of the NPs was controlled by adjusting the ratio of OLA to toluene or by changing the reaction temperature.

Synthesis of 2.58 nm gold nanoparticles: $HAuCl_4 \cdot 3H_2O$ (50 mg, 0.127 mmol) was dissolved in a mixture of toluene (2 mL) and OLA (2 mL). Then, a solution of BTBA (43 mg, 0.5 mmol) in a mixture of toluene (0.5 mL) and OLA (0.5 mL) was quickly injected into the Au(III) solution at 40 ºC under nitrogen atmosphere with vigorous stirring. The color of the mixture immediately changed from orange to brown. After 5 min, the water bath was removed and stirring was continued at room temperature for 1 h. Then, ethanol (30 mL) was added to induce precipitation of gold NPs. The NPs were collected by centrifugation, redispersed in toluene (2 mL), and precipitated again with ethanol (10 mL). After the redispersion–precipitation cycle was repeated twice, the NPs were redispersed in toluene (10 mL). NP diameter = 2.58±0.27 nm.

Synthesis of 2.92 nm gold nanoparticles: $HAuCl_4 \cdot 3H_2O$ (50 mg, 0.127 mmol) was dissolved in a mixture of toluene (2.4 mL) and OLA (1.6 mL). The resulting mixture was brought to 40 ºC using a water bath and a solution of BTBA (43 mg, 0.5 mmol) in a mixture of toluene (0.6 mL), and OLA (0.4 mL) was injected all at once under nitrogen atmosphere with vigorous stirring. The color of the mixture immediately changed from orange to brown. After 5 min, the water bath was removed and stirring was continued at room temperature for 1 h. Then, ethanol (30 mL) was added to induce the precipitation of gold NPs. The NPs were collected by centrifugation, redispersed in toluene (2 mL), and precipitated again with ethanol (10 mL). After the redispersion–precipitation cycle was repeated twice, the NPs were redispersed in toluene (10 mL). NP diameter = 2.92±0.33 nm.

Synthesis of 3.73 nm gold nanoparticles: $HAuCl_4 \cdot 3H_2O$ (50 mg, 0.127 mmol) was dissolved in a mixture of toluene (2 mL) and OLA (2 mL). Then, a solution of BTBA (43 mg, 0.5 mmol) in a mixture of toluene (0.5 mL) and OLA (0.5 mL) was injected all at once into the Au(III) solution at room temperature (23 ºC) under nitrogen atmosphere with vigorous stirring. The color of the mixture immediately changed from orange to dark red; stirring was continued for an additional hour. Then, ethanol (30 mL) was added to induce the precipitation of gold NPs. The NPs were collected by centrifugation, redispersed in toluene (2 mL) and precipitated again with ethanol (10 mL). After the redispersion–precipitation cycle was repeated twice, the NPs were redispersed in toluene (10 mL). NP diameter = 3.73±0.32 nm.

Synthesis of 4.19 nm gold nanoparticles: $HAuCl_4 \cdot 3H_2O$ (50 mg, 0.127 mmol) was dissolved in a mixture of toluene (2 mL) and OLA (2 mL). The resulting solution was cooled to 3 ºC and a solution of BTBA (43 mg, 0.5 mmol) in a mixture of toluene (0.5 mL) and OLA (0.5 mL) was injected all at once under nitrogen atmosphere with vigorous stirring. The color of the mixture immediately changed from orange to dark red. After 5 min, the ice bath was removed and stirring was continued at room temperature for 1 h. Then, ethanol (30 mL) was added to induce the precipitation of gold NPs. The NPs were collected by centrifugation, redispersed in toluene (2 mL) and precipitated again with ethanol (10 mL). After the redispersion–precipitation cycle was repeated twice, the NPs were redispersed in toluene (10 mL). NP diameter = 4.19±0.35 nm.

- Size-uniform gold nanoparticles with sizes in the range 4.34–5.28 nm were synthesized by seeded growth using 3.73±0.32 nm NPs as the seeds.

Synthesis of 4.34 nm gold nanoparticles: $HAuCl_4 \cdot 3H_2O$ (18.3 mg, 0.046 mmol) was dissolved in a mixture of toluene (0.9 mL) and OLA (0.9 mL). Then, 6.35 mL of a toluene solution of 3.73 nm Au NPs (see above) and an additional 6.35 mL of OLA were added, and the reaction mixture was stirred overnight at 60 ºC. Thereafter, ethanol (30 mL) was added to induce the precipitation of the enlarged gold NPs. The NPs were collected by centrifugation, redispersed in toluene (2 mL), and precipitated again with ethanol (10 mL). After the redispersion–precipitation cycle was repeated twice, the NPs were redispersed in toluene (10 mL). NP diameter = 4.34±0.35 nm.

Synthesis of 4.53 nm gold nanoparticles: $HAuCl_4 \cdot 3H_2O$ (22.1 mg, 0.056 mmol) was dissolved in a mixture of toluene (1.1 mL) and OLA (1.1 mL). Then, 5.58 mL of a toluene solution of 3.73 nm Au NPs (see above) and an additional 5.58 mL of OLA were added, and the reaction mixture was stirred overnight at 60 ºC. Thereafter, ethanol (30 mL) was added to induce the precipitation of the enlarged gold NPs. The NPs were collected by centrifugation, redispersed in toluene (2 mL), and precipitated again with ethanol (10 mL). After the redispersion–precipitation cycle was repeated twice, the NPs were redispersed in toluene (10 mL). NP diameter = 4.53±0.43 nm.

Synthesis of 4.72 nm gold nanoparticles: $HAuCl_4 \cdot 3H_2O$ (25.3 mg, 0.064 mmol) was dissolved in a mixture of toluene (1.25 mL) and OLA (1.25 mL). Then, 4.94 mL of a toluene solution of 3.73 nm Au NPs (see above) and an additional 4.94 mL of OLA were added, and the reaction mixture was stirred overnight at 60 ºC. Thereafter, ethanol (30 mL) was added to induce the precipitation of the enlarged gold NPs. The NPs were collected by centrifugation, redispersed in toluene (2 mL), and precipitated again with ethanol (10 mL). After the redispersion–precipitation cycle was repeated twice, the NPs were redispersed in toluene (10 mL). NP diameter = 4.72±0.37 nm.

Synthesis of 5.28 nm gold nanoparticles: $HAuCl_4 \cdot 3H_2O$ (32.4 mg, 0.082 mmol) was dissolved in a mixture of toluene (1.6 mL) and OLA (1.6 mL). Then, 3.24 mL of a toluene solution of 3.73 nm Au NPs (see above) and an additional 3.24 mL of OLA were added, and the reaction mixture was stirred overnight at 60 ºC. Thereafter, ethanol (30 mL) was added to induce the precipitation of the enlarged gold NPs. The NPs were collected by centrifugation, redispersed in toluene (2 mL), and precipitated again with ethanol (10 mL). After the redispersion–precipitation cycle was repeated twice, the NPs were redispersed in toluene (10 mL). NP diameter = 5.28±0.37 nm.

- Size-uniform gold nanoparticles with sizes in the range 5.37–8.48 nm were synthesized by seeded growth using 4.19±0.35 nm NPs as the seeds.

Synthesis of 5.37 nm gold nanoparticles: $HAuCl_4 \cdot 3H_2O$ (26.2 mg, 0.067 mmol) was dissolved in a mixture of toluene (1.3 mL) and OLA (1.3 mL). Then, 4.75 mL of a toluene solution of 4.19 nm Au NPs (see above) and an additional 4.75 mL of OLA were added, and the reaction mixture was stirred overnight at 60 ºC. Thereafter, ethanol (30 mL) was added to induce the precipitation of the enlarged gold NPs. The NPs were collected by centrifugation, redispersed in toluene (2 mL), and precipitated again with ethanol (10 mL). After the redispersion–precipitation cycle was repeated twice, the NPs were redispersed in toluene (10 mL). NP diameter = 5.37±0.37 nm.

Synthesis of 5.63 nm gold nanoparticles: $HAuCl_4 \cdot 3H_2O$ (29.4 mg, 0.075 mmol) was dissolved in a mixture of toluene (1.5 mL) and OLA (1.5 mL). Then, 4.12 mL of a toluene solution of 4.19 nm Au NPs (see above), an additional 1 mL of toluene, and an additional 5.12 mL of OLA were added and the reaction mixture was stirred overnight at 60 ºC. Thereafter, ethanol (30 mL) was added to induce the precipitation of the enlarged gold NPs. The NPs were collected by centrifugation, redispersed in toluene (2 mL), and precipitated again with ethanol (10 mL). After the redispersion–precipitation cycle was repeated twice, the NPs were redispersed in toluene (10 mL). NP diameter = 5.63±0.45 nm.

Synthesis of 5.78 nm gold nanoparticles: $HAuCl_4 \cdot 3H_2O$ (31.9 mg, 0.080 mmol) was dissolved in a mixture of toluene (1.6 mL) and OLA (1.6 mL). Then, 3.81 mL of a toluene solution of 4.19 nm Au NPs (see above), an additional 2 mL of toluene, and an additional 5.81 mL of OLA were added and the reaction mixture was stirred overnight at 60 ºC. Thereafter, ethanol (30 mL) was added to induce the precipitation of the enlarged gold NPs. The NPs were collected by centrifugation, redispersed in toluene (2 mL), and precipitated again with ethanol (10 mL). After the redispersion–precipitation cycle was repeated twice, the NPs were redispersed in toluene (10 mL). NP diameter = 5.78±0.38 nm.

Synthesis of 6.05 nm gold nanoparticles: $HAuCl_4 \cdot 3H_2O$ (34.0 mg, 0.086 mmol) was dissolved in a mixture of toluene (1.7 mL) and OLA (1.7 mL). Then, 3.32 mL of a toluene solution of 4.19 nm Au NPs (see above), an additional 2 mL of toluene, and an additional 5.32 mL of OLA were added and the reaction mixture was stirred overnight at 60 ºC. Thereafter, ethanol (30 mL) was added to induce the precipitation of the enlarged gold NPs. The NPs were collected by centrifugation, redispersed in toluene (2 mL), and precipitated again with ethanol (10 mL). After the redispersion–precipitation cycle was repeated twice, the NPs were redispersed in toluene (10 mL). NP diameter = 6.05±0.52 nm.

Synthesis of 6.86 nm gold nanoparticles: $HAuCl_4 \cdot 3H_2O$ (39.6 mg, 0.101 mmol) was dissolved in a mixture of toluene (2 mL) and OLA (2 mL). Then, 2.28 mL of a toluene solution of 4.19 nm Au NPs (see above), an additional 3 mL of toluene, and an additional 5.28 mL of OLA were added and the reaction mixture was stirred overnight at 60 ºC. Thereafter, ethanol (30 mL) was added to induce the precipitation of the enlarged gold NPs. The NPs were collected by centrifugation, redispersed in toluene (2 mL), and precipitated again with ethanol (10 mL). After the redispersion–precipitation cycle was repeated twice, the NPs were redispersed in toluene (10 mL). NP diameter = 6.86±0.46 nm.

Synthesis of 7.38 nm gold nanoparticles: $HAuCl_4 \cdot 3H_2O$ (43.4 mg, 0.110 mmol) was dissolved in a mixture of toluene (2.2 mL) and OLA (2.2 mL). Then, 1.83 mL of a toluene solution of 4.19 nm Au NPs (see above), an additional 3 mL of toluene and an additional 4.83 mL of OLA were added, and the reaction mixture was stirred overnight at 60 ºC. Thereafter, ethanol (30 mL) was added to induce the precipitation of the enlarged gold NPs. The NPs were collected by centrifugation, redispersed in toluene (2 mL), and precipitated again with ethanol (10 mL). After the redispersion–precipitation cycle was repeated twice, the NPs were redispersed in toluene (10 mL). NP diameter = 7.38±0.62 nm.

Synthesis of 7.48 nm gold nanoparticles: $HAuCl_4 \cdot 3H_2O$ (44.1 mg, 0.112 mmol) was dissolved in a mixture of toluene (2.3 mL) and OLA (2.3 mL). Then, 1.76 mL of a toluene solution of 4.19 nm Au NPs (see above), an additional 3 mL of toluene, and an additional 4.76 mL of OLA were added and the reaction mixture was stirred overnight at 60 ºC. Thereafter, ethanol (30 mL) was added to induce the precipitation of the enlarged gold NPs. The NPs were collected by centrifugation, redispersed in toluene (2 mL), and precipitated again with ethanol (10 mL). After the redispersion–precipitation cycle was repeated twice, the NPs were redispersed in toluene (10 mL). NP diameter = 7.48±0.60 nm.

Synthesis of 8.48 nm gold nanoparticles: $HAuCl_4 \cdot 3H_2O$ (47.2 mg, 0.120 mmol) was dissolved in a mixture of toluene (2.3 mL) and OLA (2.3 mL). Then, 1.21 mL of a toluene solution of 4.19 nm Au NPs (see above), an additional 4 mL of toluene, and an additional 5.21 mL of OLA were added and the reaction mixture was stirred overnight at 60 ºC. Thereafter, ethanol (30 mL) was added to induce the precipitation of the enlarged gold NPs. The NPs were collected by centrifugation, redispersed in toluene (2 mL), and precipitated again with ethanol (10 mL). After the redispersion–precipitation cycle was repeated twice, the NPs were redispersed in toluene (10 mL). NP diameter = 8.48±0.51 nm.

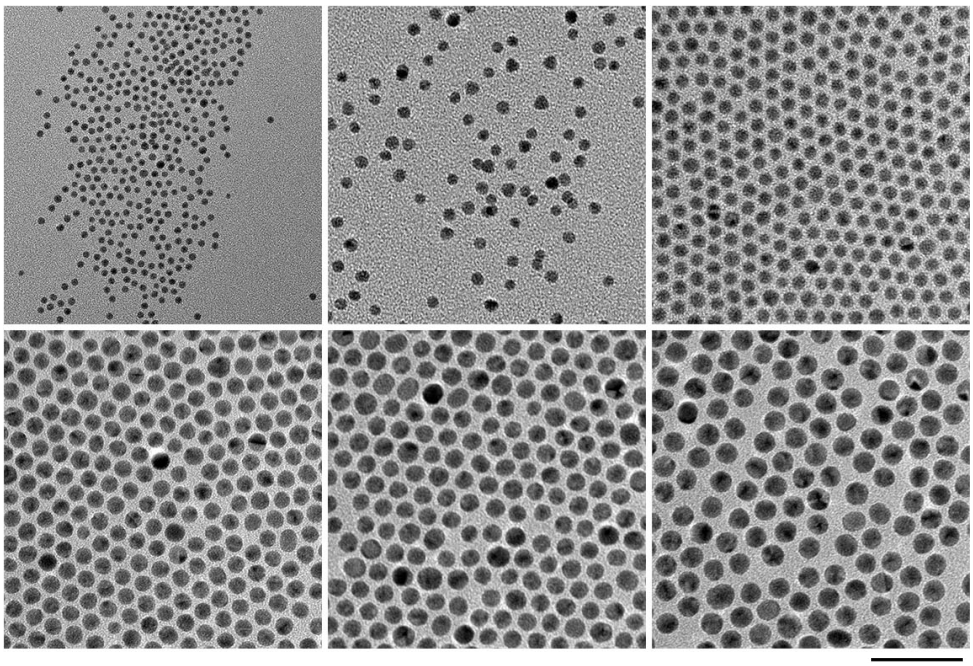

Supplementary Fig. 1 | Representative TEM images of as-synthesized (OLA-capped) Au NPs. NP diameters: top row, from the left: 3.73±0.32 nm, 4.69±0.39 nm, and 5.37±0.37 nm; bottom row, from the left: 6.86±0.46 nm, 7.38±0.62 nm, and 8.48±0.51 nm. Scale bar = 50 nm.

- Size-uniform palladium nanoparticles were synthesized by reducing $PdCl_2$ with borane–*tert*-butylamine (BTBA) complex in toluene in the presence of OLA, by modifying a previously reported procedure[2]. The size of the NPs was controlled by changing the reaction temperature.

Synthesis of 3.90 nm palladium nanoparticles: $PdCl_2$ (88 mg, 0.50 mmol) was dissolved in a mixture of toluene (4 mL) and OLA (4 mL) preheated to 60 ºC using a water bath. The temperature was decreased to 40 ºC and a solution of BTBA (174 mg, 2 mmol) in a mixture of toluene (1 mL) and OLA (1 mL) was injected all at once under nitrogen atmosphere with vigorous stirring. The color of the mixture immediately turned dark. After 5 min, the water bath was removed and stirring was continued at room temperature for 1 h. Then, ethanol (30 mL) was added to induce the precipitation of palladium NPs. The NPs were collected by centrifugation, redispersed in toluene (2 mL), and precipitated again with ethanol (10 mL). After the redispersion–precipitation cycle was repeated twice, the NPs were redispersed in toluene (20 mL). NP diameter = 3.90±0.40 nm.

Synthesis of 4.15 nm palladium nanoparticles: $PdCl_2$ (88 mg, 0.50 mmol) was dissolved in a mixture of toluene (4 mL) and OLA (4 mL) preheated to 60 ºC using a water bath. The resulting solution was cooled down to 3 ºC using an ice bath and a solution of BTBA (174 mg, 2 mmol) in a mixture of toluene (1 mL), and OLA (1 mL) was injected all at once under nitrogen atmosphere with vigorous stirring. The color of the mixture immediately turned dark. After 5 min, the ice bath was removed and stirring was continued at room temperature for 1 h. Then, ethanol (30 mL) was added to induce the precipitation of palladium NPs. The NPs were collected by centrifugation, redispersed in toluene (2 mL), and precipitated again with ethanol (10 mL). After the redispersion–precipitation cycle was repeated twice, the NPs were redispersed in toluene (20 mL). NP diameter = 4.15±0.42 nm.

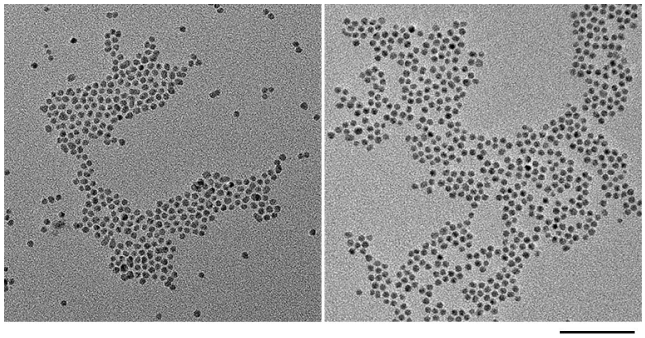

Supplementary Fig. 2 | Representative TEM images of as-synthesized (OLA-capped) Pd NPs. NP diameters, left: 3.90±0.40 nm; right: 4.15±0.42 nm. Scale bar = 50 nm.

1.2. Functionalization of gold and palladium nanoparticles with charged ligands

- Negatively charged gold nanoparticles (Au·MUA) were prepared by incubating OLA-stabilized Au NPs with 5 eq of 11-mercaptoundecanoic acid (MUA), followed by purification (5 eq of MUA corresponds to a 5-fold excess with respect to the number of binding sites on gold NPs, assuming that a single thiolate occupies[3] a surface area of 0.214 nm^2). We verified that the ligand exchange procedure did not affect the NPs' size and size dispersity.

Functionalization of 2.58 nm gold nanoparticles: To 2.0 mL of OLA-stabilized 2.58 nm Au NPs in toluene (~2.5 mg/mL) was added a solution of 5.1 mg MUA (5 eq) in a mixture of ethanol (5 mL) and toluene (3 mL) and the mixture was vigorously shaken for 4 h. The resulting precipitate was collected by centrifugation and washed with ethanol (5 mL). The NPs were redispersed in a mixture of 25% methanolic solution of NMe_4OH (20 μL) and water (100 μL), reprecipitated using acetone (5 mL), and collected by centrifugation. The redispersion/precipitation procedure was repeated twice. Finally, the NPs were redispersed in 5 mL of deionized water (the pH of the final solution was ~11 due to residual NMe_4OH).

Functionalization of 2.92 nm gold nanoparticles: Analogous to 2.58 nm gold nanoparticles, except that 4.5 mg of MUA (5 eq) was used.

Functionalization of 3.73 nm gold nanoparticles: Analogous to 2.58 nm gold nanoparticles, except that 3.5 mg of MUA (5 eq) was used.

Functionalization of 4.19 nm gold nanoparticles: Analogous to 2.58 nm gold nanoparticles, except that 3.1 mg of MUA (4.9 eq) was used.

Functionalization of 4.34 nm gold nanoparticles: Analogous to 2.58 nm gold nanoparticles, except that 3.0 mg of MUA (5 eq) was used.

Functionalization of 4.53 nm gold nanoparticles: Analogous to 2.58 nm gold nanoparticles, except that 2.9 mg of MUA (5 eq) was used.

Functionalization of 4.72 nm gold nanoparticles: Analogous to 2.58 nm gold nanoparticles, except that 2.8 mg of MUA (5 eq) was used.

Functionalization of 5.28 nm gold nanoparticles: Analogous to 2.58 nm gold nanoparticles, except that 2.5 mg of MUA (5 eq) was used.

Functionalization of 5.37 nm gold nanoparticles: Analogous to 2.58 nm gold nanoparticles, except that 2.5 mg of MUA (5.1 eq) was used.

Functionalization of 5.63 nm gold nanoparticles: Analogous to 2.58 nm gold nanoparticles, except that 2.4 mg of MUA (5.1 eq) was used.

Functionalization of 5.78 nm gold nanoparticles: Analogous to 2.58 nm gold nanoparticles, except that 2.3 mg of MUA (5.1 eq) was used.

Functionalization of 6.05 nm gold nanoparticles: Analogous to 2.58 nm gold nanoparticles, except that 2.2 mg of MUA (5.1 eq) was used.

Functionalization of 6.86 nm gold nanoparticles: Analogous to 2.58 nm gold nanoparticles, except that 1.9 mg of MUA (5 eq) was used.

Functionalization of 7.38 nm gold nanoparticles: Analogous to 2.58 nm gold nanoparticles, except that 1.8 mg of MUA (5.1 eq) was used.

Functionalization of 7.48 nm gold nanoparticles: Analogous to 2.58 nm gold nanoparticles, except that 1.8 mg of MUA (5.1 eq) was used.

Functionalization of 8.48 nm gold nanoparticles: Analogous to 2.58 nm gold nanoparticles, except that 1.6 mg of MUA (5.2 eq) was used.

- Positively charged gold nanoparticles (Au·TMA) were prepared by incubating OLA-stabilized Au NPs with a mixture of 4.5 eq of (11-mercaptoundecyl)-*N,N,N*-trimethylammonium bromide (TMA; synthesized based on a previously reported procedure[4]), and 0.5 eq of 1-hexanethiol (HT), followed by purification. Without the addition of a small amount of HT, the NPs could not be fully redispersed in water, most likely because of the presence of the residual OLA (note that TMA ligands alone may not be able to form a densely packed monolayer on the NPs due to electrostatic repulsion between the positively charged terminal groups, leaving behind a small amount of the hydrophobic OLA on the NPs).

Functionalization of 2.58 nm gold nanoparticles: To 2.0 mL of OLA-stabilized 2.58 nm Au NPs in toluene (~2.5 mg/mL) was added a solution of 6.6 mg TMA (4.3 eq) and 0.28 mg HT (0.5 eq) in a mixture of ethanol (5 mL) and toluene (3 mL), and the resulting mixture was vigorously shaken for 4 h. The resulting precipitate was collected by centrifugation and redispersed in 100 μL of methanol. The NPs were precipitated using ethyl acetate (5 mL) and collected by centrifugation. The redispersion/precipitation procedure was repeated twice. Finally, the NPs were redispersed in 5 mL of deionized water.

Functionalization of 2.92 nm gold nanoparticles: Analogous to 2.58 nm gold nanoparticles, except that 5.8 mg of TMA (4.3 eq) and 0.24 mg of HT (0.5 eq) were used.

Functionalization of 3.73 nm gold nanoparticles: Analogous to 2.58 nm gold nanoparticles, except that 4.6 mg of TMA (4.3 eq) and 0.19 mg of HT (0.5 eq) were used.

Functionalization of 4.19 nm gold nanoparticles: Analogous to 2.58 nm gold nanoparticles, except that 4.1 mg of TMA (4.4 eq) and 0.17 mg of HT (0.5 eq) were used.

Functionalization of 4.34 nm gold nanoparticles: Analogous to 2.58 nm gold nanoparticles, except that 3.9 mg of TMA (4.3 eq) and 0.16 mg of HT (0.5 eq) were used.

Functionalization of 4.53 nm gold nanoparticles: Analogous to 2.58 nm gold nanoparticles, except that 3.8 mg of TMA (4.4 eq) and 0.16 mg of HT (0.5 eq) were used.

Functionalization of 4.72 nm gold nanoparticles: Analogous to 2.58 nm gold nanoparticles, except that 3.6 mg of TMA (4.3 eq) and 0.15 mg of HT (0.5 eq) were used.

Functionalization of 5.28 nm gold nanoparticles: Analogous to 2.58 nm gold nanoparticles, except that 3.2 mg of TMA (4.3 eq) and 0.14 mg of HT (0.5 eq) were used.

Functionalization of 5.37 nm gold nanoparticles: Analogous to 2.58 nm gold nanoparticles, except that 3.2 mg of TMA (4.4 eq) and 0.13 mg of HT (0.5 eq) were used.

Functionalization of 5.63 nm gold nanoparticles: Analogous to 2.58 nm gold nanoparticles, except that 3.0 mg of TMA (4.3 eq) and 0.13 mg of HT (0.5 eq) were used.

Functionalization of 5.78 nm gold nanoparticles: Analogous to 2.58 nm gold nanoparticles, except that 2.9 mg of TMA (4.3 eq) and 0.12 mg of HT (0.5 eq) were used.

Functionalization of 6.05 nm gold nanoparticles: Analogous to 2.58 nm gold nanoparticles, except that 2.8 mg of TMA (4.3 eq) and 0.12 mg of HT (0.5 eq) were used.

Functionalization of 6.86 nm gold nanoparticles: Analogous to 2.58 nm gold nanoparticles, except that 2.5 mg of TMA (4.3 eq) and 0.10 mg of HT (0.5 eq) were used.

Functionalization of 7.38 nm gold nanoparticles: Analogous to 2.58 nm gold nanoparticles, except that 2.3 mg of TMA (4.3 eq) and 0.10 mg of HT (0.5 eq) were used.

Functionalization of 7.48 nm gold nanoparticles: Analogous to 2.58 nm gold nanoparticles, except that 2.3 mg of TMA (4.4 eq) and 0.10 mg of HT (0.5 eq) were used.

Functionalization of 8.48 nm gold nanoparticles: Analogous to 2.58 nm gold nanoparticles, except that 2.0 mg of TMA (4.3 eq) and 0.09 mg of HT (0.5 eq) were used.

- Negatively charged palladium nanoparticles (Pd·MUA) were prepared by incubating OLA-stabilized Pd NPs with ~5 eq of 11-mercaptoundecanoic acid (MUA), followed by purification (we assumed that a single thiolate ligand occupies the same surface area on a Pd NP as on an Au NP).

Functionalization of 3.90 nm palladium nanoparticles: To 2.0 mL of OLA-stabilized 3.90 nm Pd NPs in toluene (~2.7 mg/mL) was added a solution of 5.4 mg MUA (4.6 eq) in a mixture of ethanol (5 mL) and toluene (3 mL), and the mixture was vigorously shaken for 4 h. The resulting precipitate was collected by centrifugation and washed with ethanol (5 mL). The NPs were redispersed in a mixture of 25% methanolic solution of NMe_4OH (20 μL) and water (100 μL), reprecipitated using acetone (5 mL), and collected by centrifugation. The redispersion/precipitation procedure was repeated twice. Finally, the NPs were redispersed in 5 mL of deionized water.

Functionalization of 4.15 nm palladium nanoparticles: Analogous to 3.90 nm palladium nanoparticles, except that 5.1 mg of MUA (4.7 eq) was used.

- Positively charged palladium nanoparticles (Pd·TMA) were prepared by incubating OLA-stabilized Pd NPs with a mixture of ~4 eq of TMA and ~0.5 eq of HT, followed by purification.

Functionalization of 3.90 nm palladium nanoparticles: To 2.0 mL of OLA-stabilized 3.90 nm Pd NPs in toluene (~2.7 mg/mL) was added a solution of 7.0 mg TMA (4.0 eq) and 0.29 mg HT (0.5 eq) in a mixture of ethanol (5 mL) and toluene (3 mL), and the resulting mixture was vigorously shaken for 4 h. The resulting precipitate was collected by centrifugation and redispersed in 100 μL of methanol. The NPs were precipitated using ethyl acetate (5 mL) and collected by centrifugation. The redispersion/precipitation procedure was repeated twice. Finally, the NPs were redispersed in 5 mL of deionized water.

Functionalization of 4.15 nm palladium nanoparticles: Analogous to 3.90 nm palladium nanoparticles, except that 6.6 mg of TMA (4.0 eq) and 0.28 mg of HT (0.5 eq) were used.

1.3. Determination of a mixed monolayer composition on the positively charged nanoparticles

All the positively charged NP were co-functionalized with TMA and a minor amount of HT. To determine the molar ratio of TMA to HT on the NPs, we adapted a previously reported procedure based on quantifying the ratio of two ligands following the oxidative dissolution of NPs with iodine[5,6]. The procedure is described here for 4.72 nm Au NPs. The NPs were functionalized as described above (Section 1.2), except that in the final step, they were not redispersed in water, but instead in DMSO-d_6 (0.6 mL). Then, 5 mg of iodine was added and the solution was sonicated in a bath sonicator for 3 min, resulting in dissolution of the NPs and liberation of the NP-bound thiolates as the corresponding disulfides. The resulting solution was transferred into an NMR tube and an ^{1}H NMR spectrum was recorded (Supplementary Fig. 3). The TMA/HT ratio was determined by integrating the signals centered at ~3.03 ppm (due to TMA's methyl protons; 9H) and at ~0.86 ppm (due to HT's methyl protons; 3H). The ratio amounted to 77:23. We note that this ratio is significantly lower than that the 90:10 "feed" ratio, indicating the preferential adsorption of HT on the NPs, which can be explained by the electrostatic repulsion between the like-charged TMA ligands on the NPs.

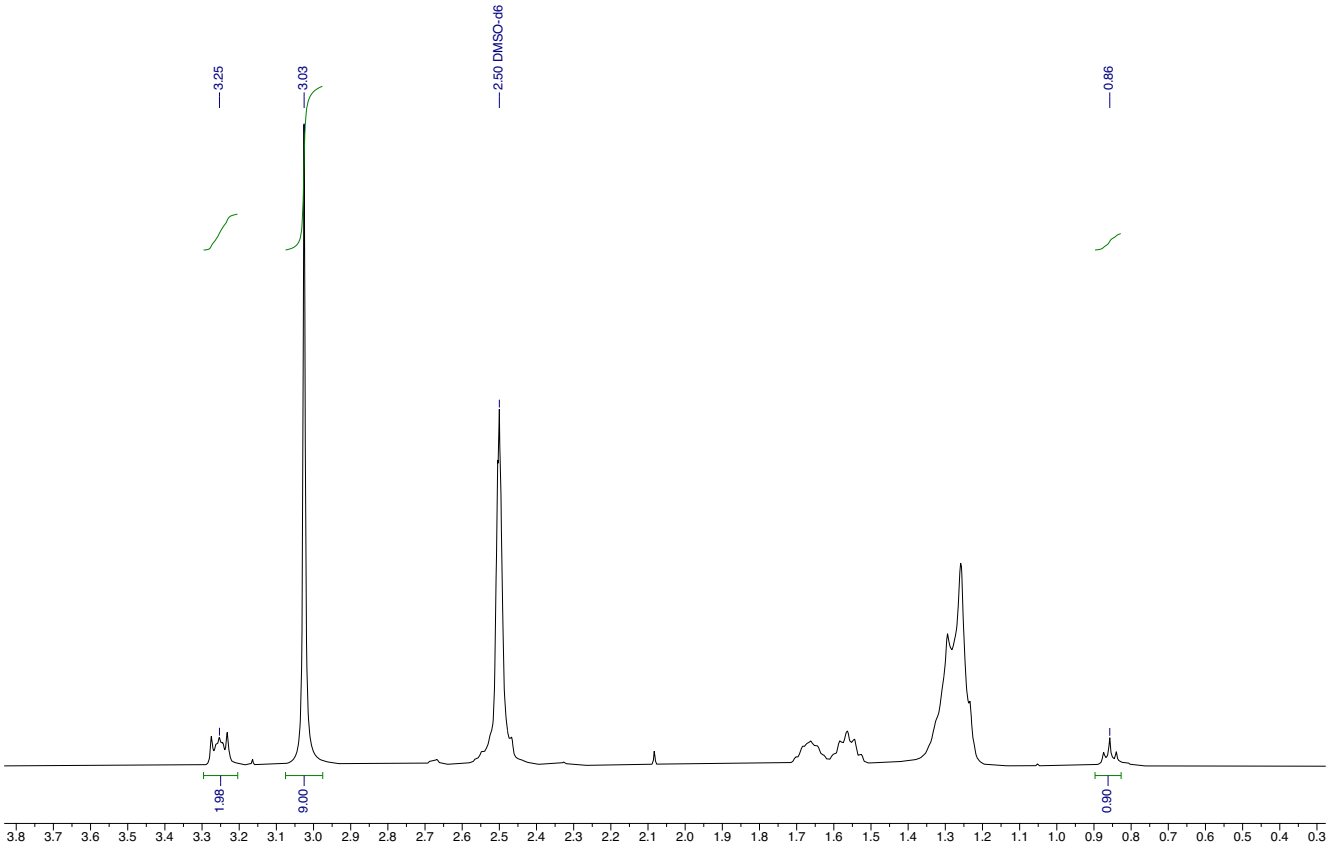

Supplementary Fig. 3 | Partial ^{1}H NMR spectrum of a solution obtained by etching TMA/HT-functionalized 4.72 nm Au NPs with iodine (400 MHz, DMSO-d_6). The signal at ~3.03 ppm originates from TMA's methyl protons (s, 9H); the signal at ~0.86 ppm originates from HT's methyl protons (t, 3H) (the signal centered at ~3.25 ppm is due to TMA's C**H**$_2$NMe$_3^+$ protons).

2. Preparation of colloidal crystals from charged nanoparticles

Colloidal crystals were prepared in a small (2 mL) glass vial by slowly decreasing the ionic strength of the solution of Au·TMA and Au·MUA during the spontaneous decomposition of $(NH_4)_2CO_3$. In a typical experiment, a solution of Au·TMA in water (200 μL, c = 1 mg/mL) was titrated with 10 μL aliquots of an aqueous solution of Au·MUA (c = 1 mg/mL, pH ≈ 11; 10 s per aliquot with vigorous shaking) until the NPs completely precipitated. The resulting aggregates were collected by centrifugation, washed with deionized water (2 × 200 μL), and dispersed in 100 μL of a saturated solution of $(NH_4)_2CO_3$ in water (c ≈ 10.4 M). The resulting solution of well-dispersed NPs was transferred to an open 2 mL glass vial and the sample was left undisturbed until the solution turned colorless and a black precipitate was observed (24–48 h; we found that the quality of the colloidal crystals could be improved by rinsing the vial with a dilute solution of Au·TMA, followed by water). The precipitate was collected by centrifugation at a low speed (~1,000 rpm), washed with deionized water (3 × 200 μL) to remove the remaining salt, and finally dispersed in ~100 μL of deionized water. For analysis by small-angle X-ray diffraction (SAXS), the suspension was placed in a borosilicate capillary tube (1.5 mm outside diameter, 0.01 mm thickness, ~80 mm in length; Charles Supper Company product # Boron-Rich 15-BG), and the tube was sealed with wax. For analysis by electron microscopy, a drop of the resulting suspension was placed on a silicon wafer (for SEM) or a carbon-coated copper grid (for TEM) and the water was evaporated.

2.1. AB-type assemblies

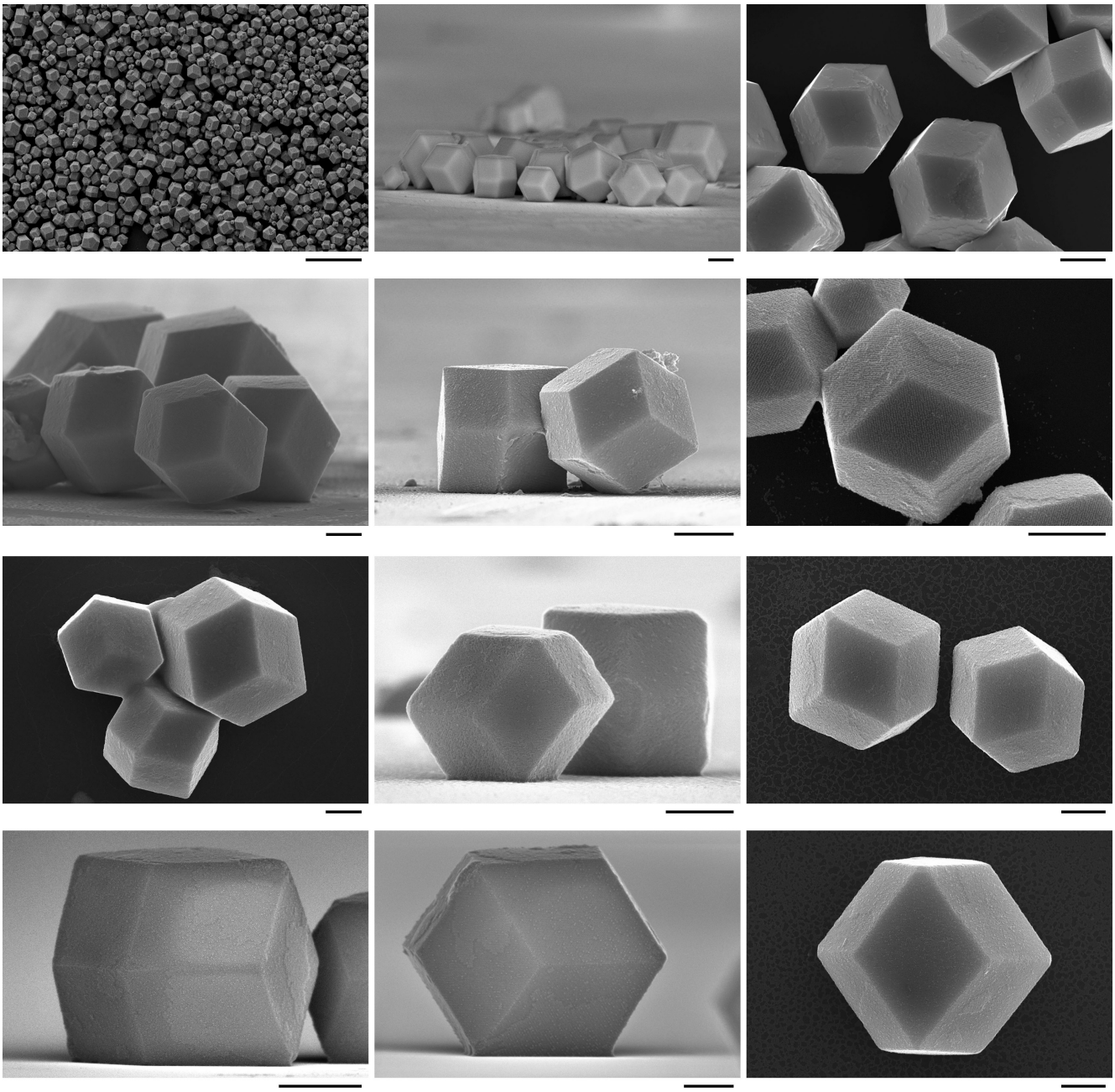

Supplementary Fig. 4 | Representative SEM images of rhombic dodecahedra with a CsCl-type structure. Building blocks, from the left: Row 1: 4.83 nm Au·TMA + 4.83 nm Au·MUA; 5.28 nm Au·TMA + 5.28 nm Au·MUA; 5.37 nm Au·TMA + 5.37 nm Au·MUA; Row 2: 5.28 nm Au·TMA + 5.28 nm Au·MUA; 5.28 nm Au·TMA + 5.28 nm Au·MUA; 7.71 nm Au·TMA + 8.23 nm Au·MUA; Row 3: 5.37 nm Au·TMA + 5.37 nm Au·MUA; 7.42 nm Au·TMA + 7.42 nm Au·MUA; 7.42 nm Au·TMA + 7.42 nm Au·MUA; Row 4: 5.37 nm Au·TMA + 5.37 nm Au·MUA; 5.28 nm Au·TMA + 5.28 nm Au·MUA; 7.42 nm Au·TMA + 7.42 nm Au·MUA. Scale bars, from the left: Row 1: 10 μm, 1 μm, 500 nm; Row 2: 500 nm, 1 μm, 500 nm; Row 3: All 500 nm; Row 4: 500 nm, 200 nm, 500 nm.

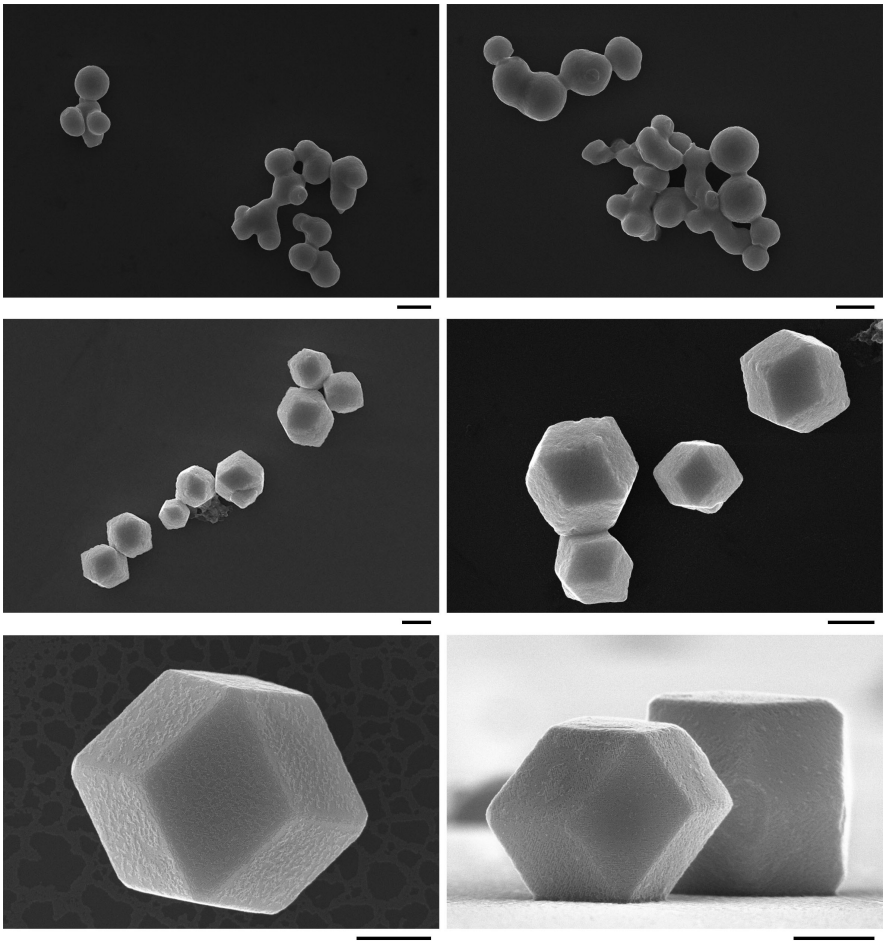

Supplementary Fig. 5 | Representative SEM images of aggregates obtained from equally sized Au·TMA and Au·MUA of the following sizes: 2.58 nm (top row; amorphous aggregates), 3.73 nm (middle row; crystalline aggregates), and 7.42 nm (bottom row; crystalline aggregates). All the self-assembly experiments were performed under the same conditions (the procedure is described at the beginning of this section; see also Fig. 1a). Scale bars (from the left): top row: 500 nm, 200 nm; middle row: 1 μm, 500 nm; bottom row: both 500 nm.

We hypothesize that the smallest NPs fail to assemble into crystalline aggregates because of the following reasons: i) The effective diameters of 2.58 nm Au·TMA and Au·MUA (i.e., the diameter of the metallic core + twice the ligand length) amount to ~5.92 nm and ~5.64 nm, respectively – i.e., only <10% of their effective volume is the hard inorganic core, with the remaining >90% being soft (the organic ligand shell) and deformable, which makes the assembly of aggregates with a long-range crystalline order more challenging; ii) NP curvature increases with decreasing NP size; therefore, the ligands on smaller NPs interact with each other less efficiently and are more disordered; iii) the size dispersity of NPs increases with decreasing NPs size, which is well illustrated by the above series: 2.58±0.27 nm, 3.73±0.32 nm, and 7.42±0.55 nm, corresponding to the dispersities of 10.5%, 8.6%, and 7.4%. The more polydisperse the NPs, the less readily they will form an ordered aggregate.

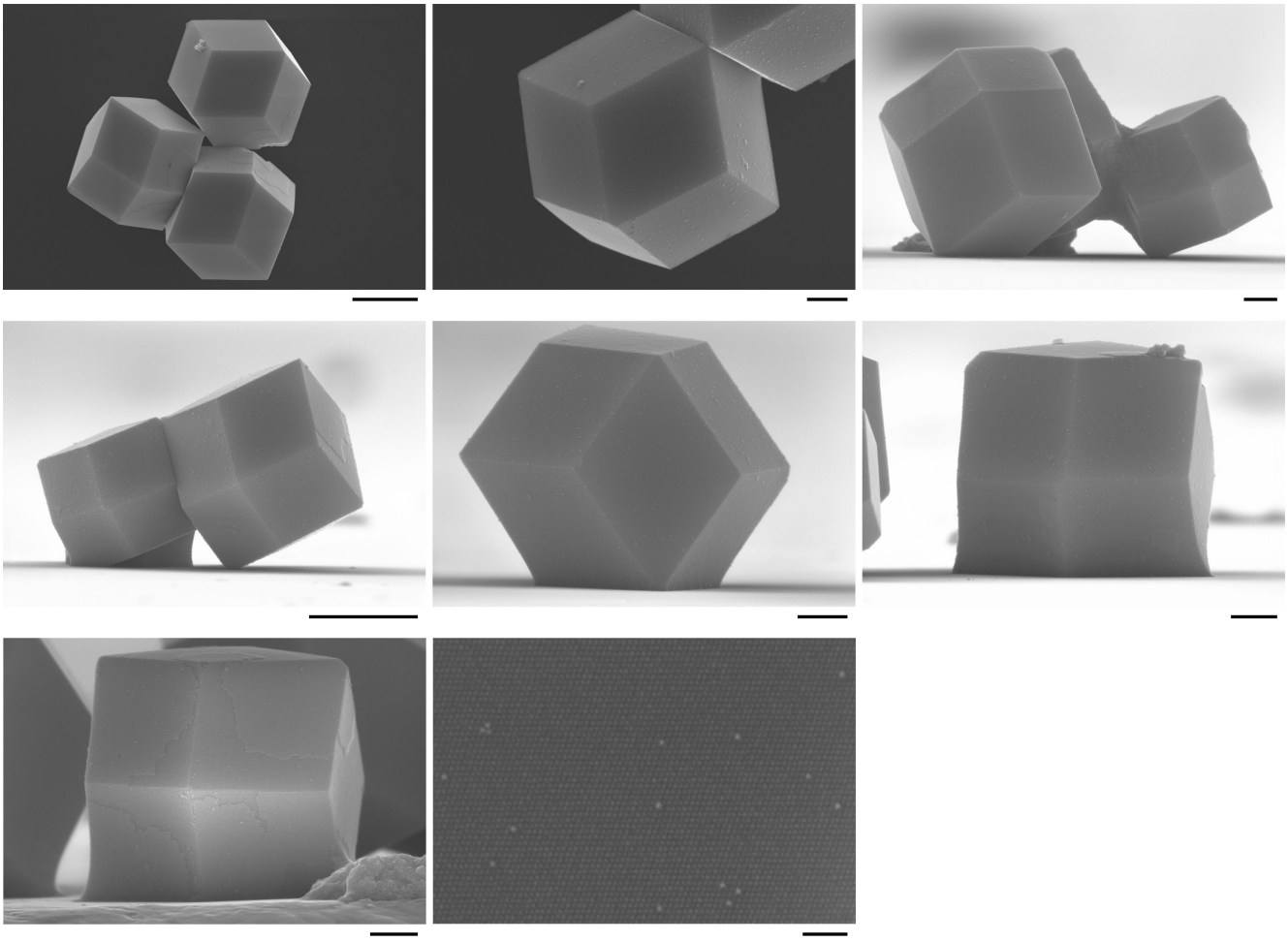

Supplementary Fig. 6 | Representative SEM images of rhombic dodecahedra obtained from equally sized Au·TMA and Au·MUA (here, 5.28 nm). Note the smooth surfaces of the colloidal crystals. Scale bars, from the left: top row: 1 μm, 200 nm, and 200 nm; middle row: 500 nm, 200 nm, and 200 nm; bottom row: 200 nm and 50 nm.

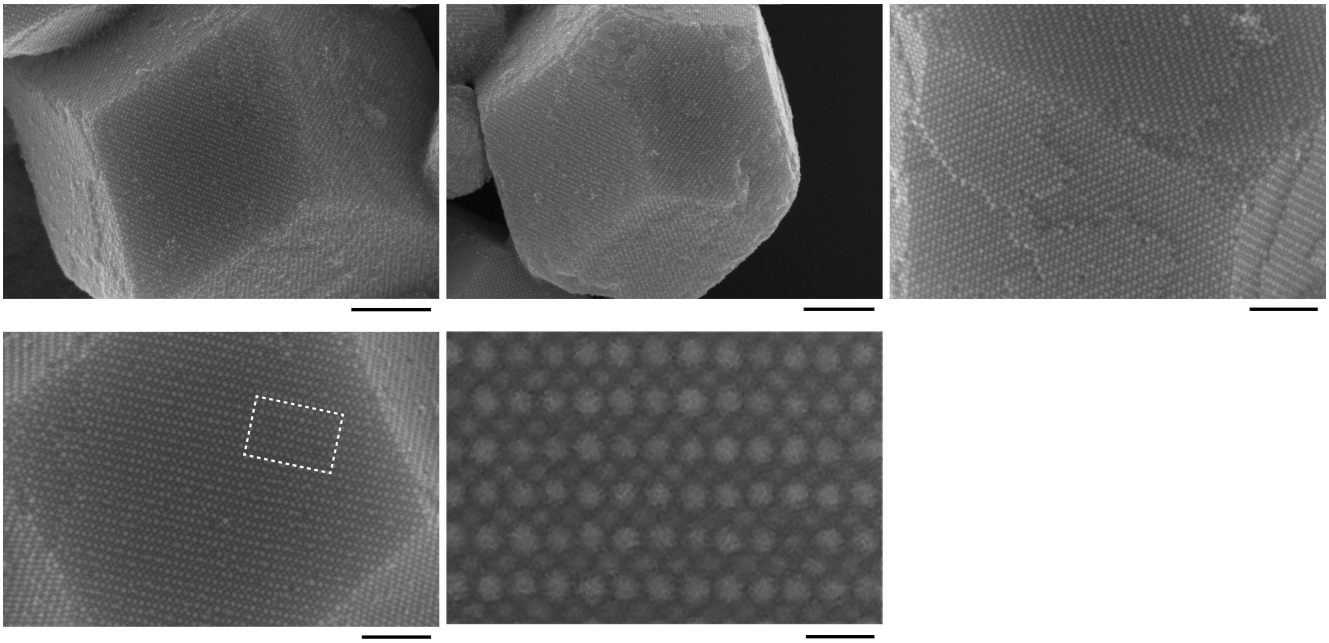

Supplementary Fig. 7 | Representative SEM images of rhombic dodecahedra obtained from differently sized Au·TMA and Au·MUA (here, 8.23 nm and 6.37 nm, respectively). The last image is a magnified view of the bottom-left image. Scale bars, from the left: top row: 200 nm, 200 nm, and 100 nm; bottom row: 100 nm and 20 nm.

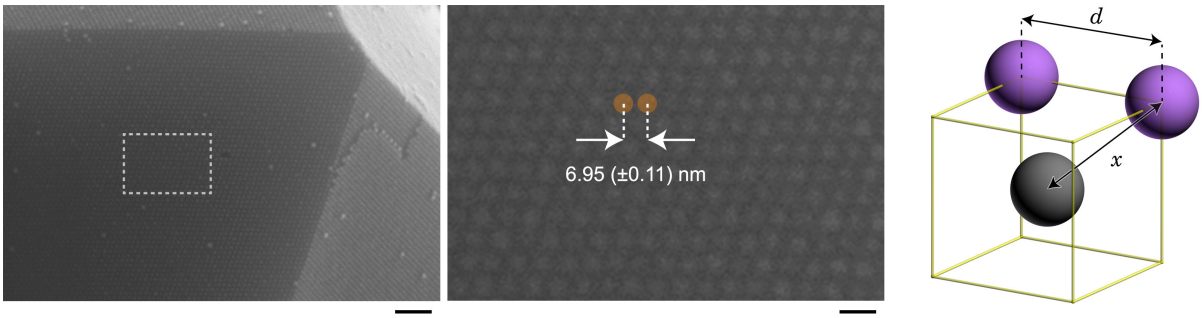

Supplementary Fig. 8 | A representative high-magnification SEM image of a rhombic dodecahedron (coassembled from equally sized, 5.28 nm Au·TMA and Au·MUA. The image on the right is a magnified view of the region indicated on the left. The center-to-center distance of 6.95±0.11 nm was determined based on multiple measurements on the surfaces of several crystals. Scale bars: left: 50 nm; right: 10 nm.

The center-to-center distance (x in the scheme on the right) corresponds to the unit cell edge length (d) of 8.02±0.12 nm, which is in agreement with the edge length determined using STEM tomography (7.93 nm; Fig. 3f, left in the main text) on a rhombic dodecahedron assembled from the same NPs.

In contrast, the center-to-center distance x determined from SAXS is considerably larger: x = 8.14 nm (based on d = 9.40 nm; Fig. 3f, right), which corresponds to a 28.6 Å gap between the surfaces of the inorganic cores. This value approaches the sum of the lengths of the two ligands in their fully extended conformations (~16.7 Å for TMA and ~15.3 Å for MUA; overall ~32.0 Å). Therefore, we conclude that the ligands on the NPs within the rhombic dodecahedra in an aqueous suspension assume extended conformations, with no interdigitation[7] (the small difference between 28.6 Å and 32.0 Å can be attributed to the NP's curvature).

Upon drying, the gap between the inorganic surfaces decreases significantly (from 28.6 Å to ~15.9 Å according to STEM tomography, and ~16.7 Å according to SEM). We note that interdigitation is unlikely, given the strong interactions between the oppositely charged tips of the TMA and MUA ligands; therefore, we conclude that the ligands' alkyl chains undergo significant compression (van der Waals collapse) upon drying.

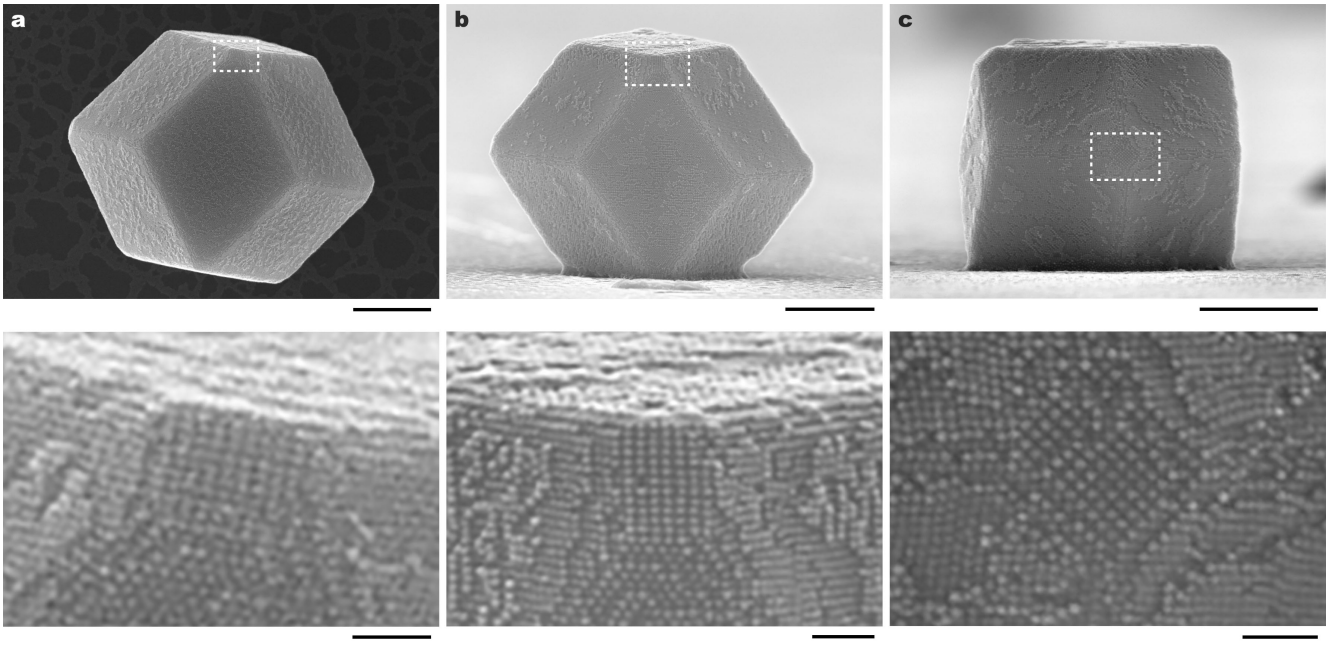

Supplementary Fig. 9 | All the 12 faces of a rhombic dodecahedron are identical, with the Miller index (110). Occasionally, however, small populations of the (100) facet can also be seen, as expected for the CsCl-type structure. The bottom-row images (scale bars = 50 nm) are magnified views of the images on top (scale bars = 500 nm). All the rhombic dodecahedra shown in this figure were coassembled from equally sized, 7.42 nm Au·TMA and Au·MUA.

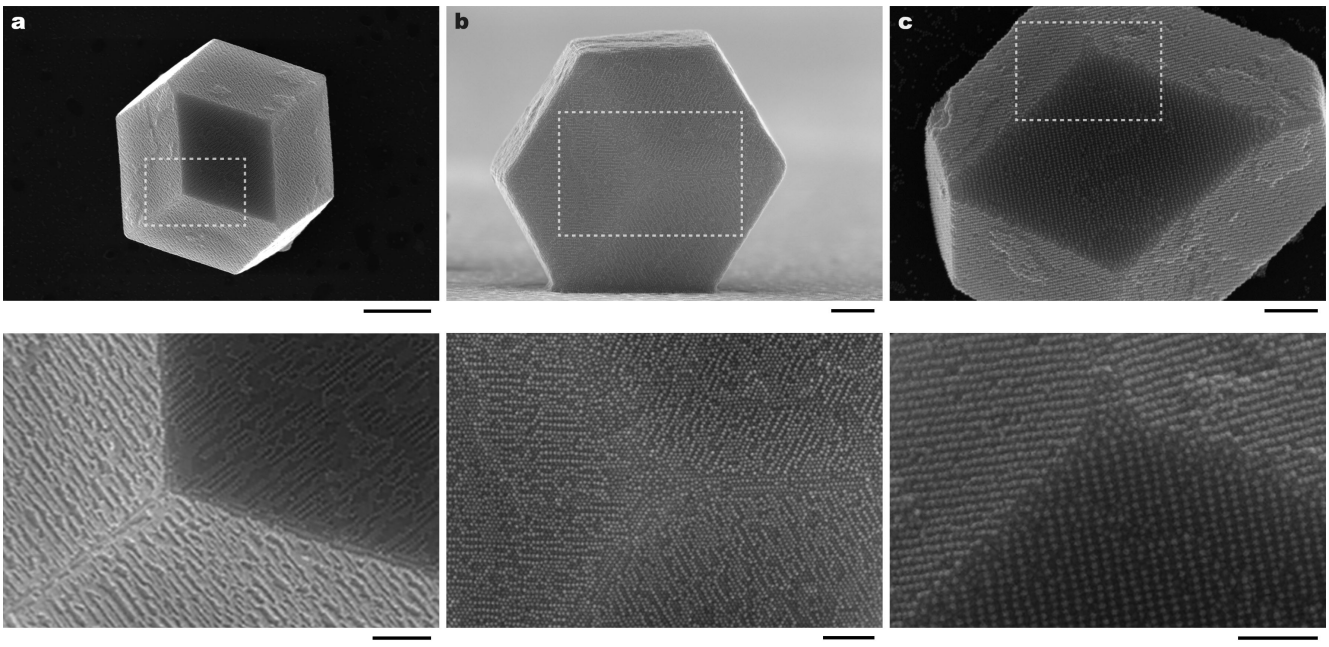

Supplementary Fig. 10 | Results of experiments, in which the rhombic dodecahedra were coassembled from a mixture of equally sized Au·TMA and Au·MUA (**a,** 5.63 nm; **b,** 7.42 nm; **c,** 8.23 nm) in the presence of a small excess of one of them. The superions used in excess attached to the oppositely charged superions comprising a (110) face of the colloidal crystal. Because the (110) face consists of alternating rows of Au·TMA and Au·MUA (see the scheme in Fig. 1a in the main text), the NPs used in excess form lines separated by a distance of 2*x* (see Supplementary Fig. 8). In this way, NPs of either charge can be mapped on the surfaces of these colloidal crystals. Scale bars: **a,** 500 nm (top) and 50 nm (bottom); **b,** 200 nm (top) and 100 nm (bottom); **c,** 200 nm (top) and 100 nm (bottom).

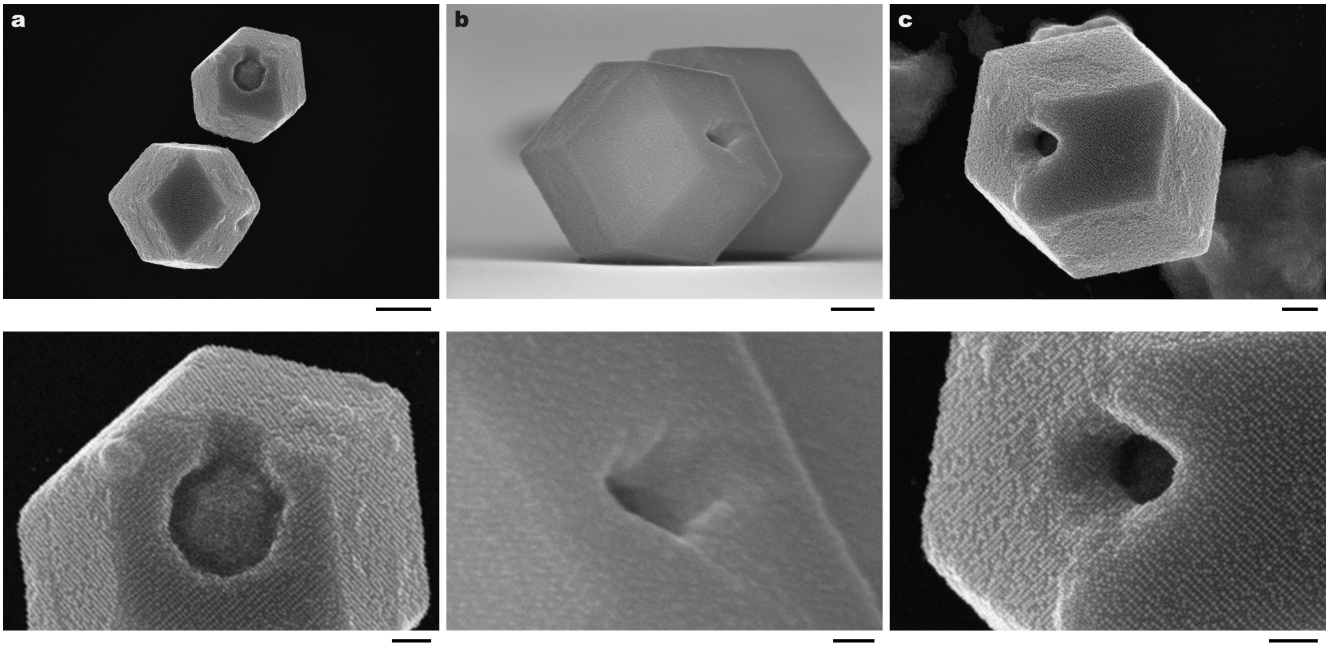

Supplementary Fig. 11 | SEM images of rhombic dodecahedra with cavities on their surfaces (the images in the bottom row are magnified views of those in the top row). We hypothesize that these cavities form as a result of the decomposition of $(NH_4)_2CO_3$ trapped within rhombic dodecahedra. Co-assembly of Au·TMA and Au·MUA having different amounts of TMA and MUA must be accompanied by entrapment of small ions (NH_4^+ and CO_3^{2-}) for the electroneutrality of the colloidal crystals. However, since self-assembly begins when the concentration of $(NH_4)_2CO_3$ is still high (4.28 M, which corresponds to an ion/NP ratio of 10^7), it is likely that both ions (NH_4^+ and CO_3^{2-}) are trapped. The trapped $(NH_4)_2CO_3$ can decompose into gaseous products (CO_2 and NH_3), which can force the formation of cavities as they escape the crystal. Similar features were observed in triakis tetrahedra (Supplementary Fig. 14). Scale bars: **a,** 500 nm and 100 nm in the magnified view; **b,** 200 nm and 50 nm in the magnified view; **c,** 200 nm and 100 nm in the magnified view. The crystals were prepared from equally sized Au·TMA and Au·MUA (7.48 nm for **a** and **c**; 5.37 nm for **b**).

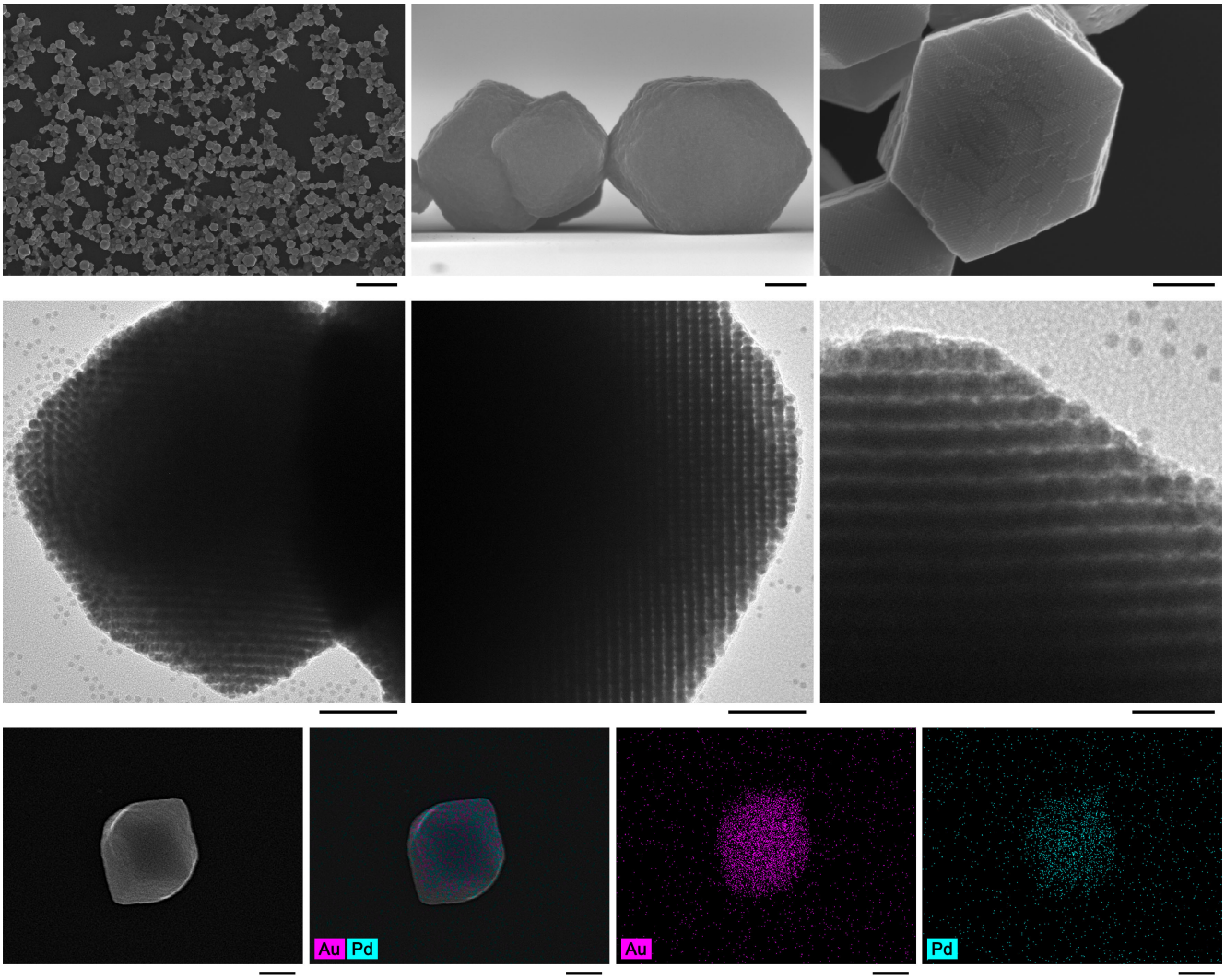

Supplementary Fig. 12 | *Top row:* Representative SEM images of rhombic dodecahedra coassembled from a 1:1 mixture of Pd·TMA and Au·MUA. *Middle row:* Representative TEM images of rhombic dodecahedra coassembled from a 1:1 mixture of Pd·TMA and Au·MUA. All the rhombic dodecahedra shown here were coassembled from 3.90 nm Pd·TMA and 5.07 nm Au·MUA (except the sample in the top-right image, which was coassembled from 4.15 nm Pd·TMA and 5.37 nm Au·MUA). *Bottom row:* Energy-dispersive spectroscopy (EDS) elemental mapping of a single rhombic dodecahedron. Elemental analysis of the rhombic dodecahedron crystal showed that the Au/Pd molar ratio within this rhombic dodecahedron corresponds to 1.90, which is in very close agreement with the calculated ratio of 1.91 (assuming NP core sizes of 5.07 nm for Au and 3.90 nm for Pd, atomic weights of 106.4 for Pd and 197 for Au, and densities of 12 g/cm^3 for Pd and 19.3 g/cm^3 for Au). Scale bars, from the left: top row: 5 μm, 200 nm, 200 nm; middle row: 50 nm, 50 nm, and 20 nm; bottom row: all 200 nm.

2.2. A_3B_4-type assemblies

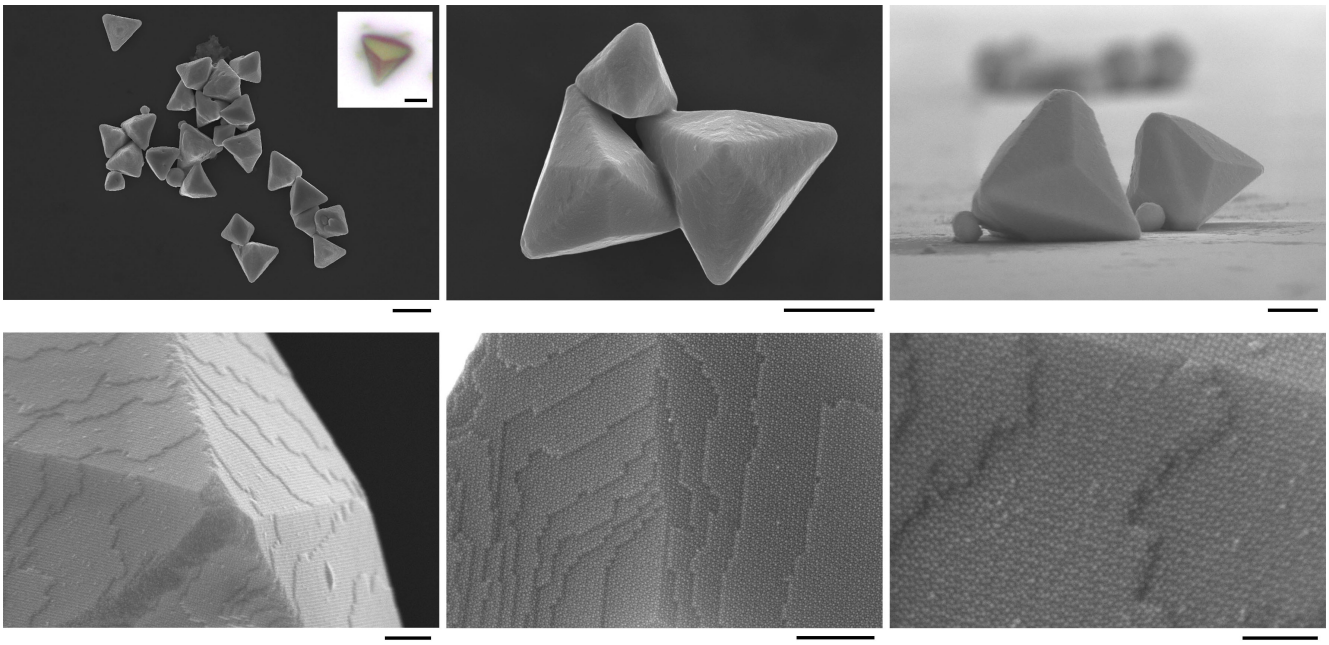

Supplementary Fig. 13 | SEM images of triakis tetrahedra with a Th_3P_4-type structure. Building blocks, from the left: top row: 2.58 nm Au·TMA + 4.73 nm Au·MUA (inset: 5.28 nm Au·TMA + 3.73 nm Au·MUA), 2.58 nm Au·TMA + 4.19 nm Au·MUA, 5.63 nm Au·TMA + 3.73 nm Au·MUA; bottom row: 6.86 nm Au·TMA + 4.39 nm Au·MUA, 5.28 nm Au·TMA + 3.73 nm Au·MUA, 6.86 nm Au·TMA + 4.39 nm Au·MUA. Scale bars (from the left): top row: 2 μm (including the inset), 1 μm, 1 μm; bottom row: 200 nm, 200 nm, 100 nm.

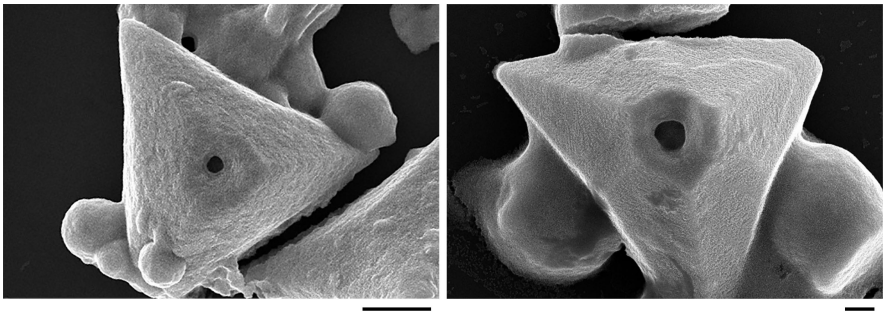

Supplementary Fig. 14 | SEM images of triakis tetrahedra with cavities on their surfaces (see also Supplementary Fig. 11). The crystals were co-assembled from 8.23 nm Au·TMA and 3.87 nm Au·MUA (left) and 7.57 nm Au·TMA and 2.12 nm Au·MUA (right) (the very small 2.12 nm Au NPs were synthesized analogously to 2.58 nm Au NPs (see Section 1.1 above), except that they were precipitated 5 min after the addition of the reducing agent). Scale bars correspond to 500 nm (left) and 200 nm (right).

3. Molecular dynamics simulations

To determine the Gibbs free-energies of attractive and repulsive coupling of pairs of NPs used in the experiments. we first prepared atomistic models of Au·MUA (5 nm Au core functionalized by 382 MUA ligands) and Au·TMA (5 nm Au core functionalized with a 7:3 mixture of TMA and hexanethiol (HT) ligands (267 and 115, respectively)[8-10]. Both models featured roughly spherical Au cores with randomly distributed thiolate ligands. The NPs were modeled in pairs (Au·TMA + Au·MUA, Au·MUA + Au·MUA, and Au·TMA + Au·TMA; Fig. 1d, Supplementary Fig. 15a, and Supplementary Fig. 15b, respectively) in $(NH_4)_2CO_3$ solution at a concentration (4.28 M) matching that corresponding to the onset of NP self-assembly in a typical experiment. The solvent molecules (TIP3P water) were prepared using the VMD Solvate plugin. The $(NH_4)_2CO_3$ solution was prepared by a combination of the VMD Autoionize plugin[11] and our own code. Free energies were obtained using umbrella sampling (US) and the weighted histogram analysis method (WHAM)[12,13].

Molecular dynamics (MD) simulations were performed using NAMD2.12 software[14]. The NP ligands and solvent molecules were described with the generalized CHARMM force field[15,16] and the parameters were determined via the CGenFF ParamChem web interface[17]. The NP core atom parameters had little influence on the NP–solvent and the NP–NP interactions, since the core atoms were fully covered by ligands. In all the simulations, the Particle Mesh Ewald (PME) method[18] was used to evaluate the long-range Coulomb interactions. The time step was set to 1.8 fs and long-range interactions were evaluated every one (van der Waals) or two (Coulombic) time steps. After 2,000 steps of minimization, solvent molecules were equilibrated for 1 ns around the NPs, which were restrained using harmonic forces with a spring constant of 1 kcal/mol·Å^2. Then, the systems were equilibrated for 10 ns by MD simulations without restraints on the internal degrees of freedom while keeping the NP core centers of mass restrained to their initial positions with a spring constant of 1 kcal/mol·Å^2. The simulations were performed in the NpT (p = 1 bar) ensembles at a constant temperature (T = 310 K) and a Langevin constant, γ_{Lang} = 0.01 ps^{-1}. Images of the simulated systems were prepared using VMD.

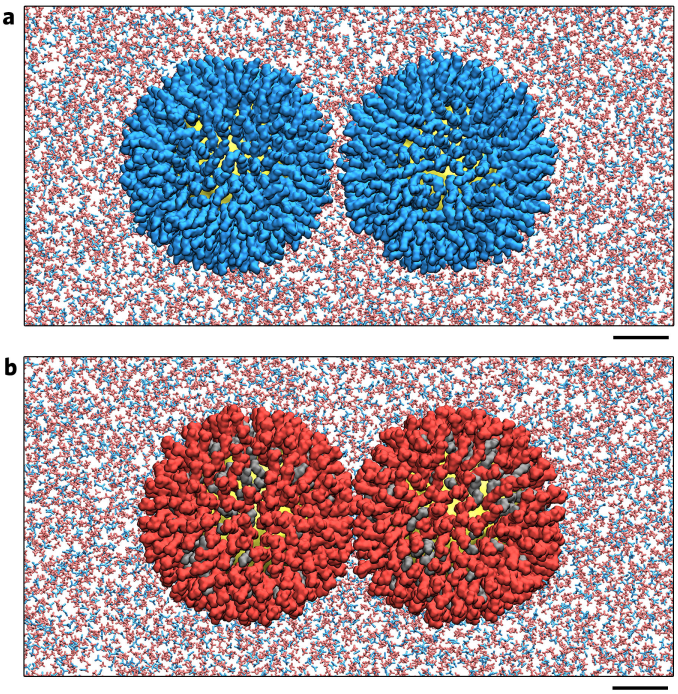

Supplementary Fig. 15 | Snapshots from atomistic simulations of **a,** two 5 nm MUA-functionalized Au NPs (Au·MUA), and **b,** two 5 nm TMA/HT-functionalized Au NPs (Au·TMA) immersed in a concentrated (4.28 M) solution of $(NH_4)_2CO_3$. The NP cores were restrained with a harmonic potential at a core-to-core distance of 7.3

nm. Simulation time = 22 ns. Color code: MUA, blue; TMA, red; HT, gray; Au core, yellow; NH_4^+, red; CO_3^{2-}, blue. Water molecules were omitted for clarity. Scale bars = 2 nm.

Gibbs free-energy calculations

The Gibbs free-energies of all three pairs of NPs (Fig. 1e in the main text) in aqueous 4.28 M $(NH_4)_2CO_3$ were determined using umbrella sampling (US) calculations. The parameters of the US calculations are reported in Supplementary Table 1. The reaction coordinate *d*, defined as the distance between the NP core centers, was partitioned into multiple (13–20) windows of 1 Å width. Occasionally, additional windows, separated by 0.5 Å from neighboring windows, were added to achieve a better histogram overlap in the US calculations. Confinement potentials were introduced in the form of harmonic restraints with force constant k. Each window was run for ~4-50 ns (details in Supplementary Table 1). The WHAM method was used to reconstruct the potential of mean force (PMF)[12,13]. The histograms of the US windows used to reconstruct the PMF were examined and shown to have an appropriate overlap.

Simulation	**Number of windows**	**Reaction coordinate centers in US windows, *d* (nm)**	**Force constants in US windows, *k* (kcal/mol·Å^2)**	**Simulation times of US windows (ns)**
Au·TMA/Au·MUA US	20	7.2, 7.3, 7.4, 7.5, 7.55, 7.6, 7.7, 7.8, 7.85, 7.9, 8.0, 8.05, 8.1, 8.2, 8.3, 8.4, 8.5, 8.6, 8.7, 8.8	10, 15, 15, 12, 10, 10, 10, 10, 10, 10, 10, 10, 10, 10, 10, 10, 10, 10, 10, 10	13.2, 21.7, 34.0, 26.3, 13.1, 26.1, 26.4, 25.1, 12.0, 25.5, 28.3, 5.3, 48.7, 17.4, 19.0, 33.7, 29.6, 20.8, 22.7, 23.4
Au·TMA/Au·TMA US	13	7.2, 7.3, 7.4, 7.5, 7.6, 7.7, 7.8, 7.9, 8.0, 8.1, 8.2, 8.3, 8.4	15, 15, 15, 15, 15, 15, 15, 15, 10, 10, 10, 10, 10	7.9, 10.0, 10.0, 9.7, 9.8, 10.0, 8.5, 15.8, 8.2, 7.5, 10.0, 8.2, 6.7
Au·MUA/Au·MUA US	16	6.7, 6.8, 6.9, 7.0, 7.1, 7.2, 7.3, 7.4, 7.5, 7.6, 7.7, 7.8, 7.9, 8.0, 8.1, 8.2	15, 15, 15, 15, 15, 15, 15, 15, 15, 10, 10, 10, 10, 10, 10, 10	5.1, 16.9, 16.7, 20.0, 8.4, 20.0, 18.5, 20.0, 19.7, 3.5, 5.9, 11.9, 20.0, 9.3, 20.0, 7.5

Supplementary Table 1 | Details of the umbrella sampling (US) simulations.

Owing to the screening effect, the interactions between the NPs are negligible unless they are in close contact (Fig. 1e). We note that upon slowly bringing two NPs together, Au·TMAs experience strong repulsion before two Au·MUAs do (red vs. blue line in Fig. 1e); this difference can be attributed to the small difference between the lengths of the two ligands (~16.7 Å for TMA and ~15.3 Å for MUA). We also note the presence of a shallow dip in the interaction potential between two Au·MUAs (the blue line in Fig. 1e), indicating a weak attractive interaction, maximized at a center-to-center distance of ~7.4 nm. This weak attraction can be induced by the NH_4^+ ions, which are present in the system at a high concentration. The NH_4^+ ions can form hydrogen bonds with MUAs' carboxylate groups, acting as a bridge between two NPs. If multiple such bridges form, the Coulombic repulsion between two Au·MUAs can be overcome by attractive intermolecular hydrogen bonding interactions. No such dip was observed in the interaction potential between two Au·TMAs (the red line in Fig. 1e) since TMA's quaternary ammonium groups cannot form hydrogen bonds with the CO_3^{2-} ions.

4. Structure determination by small-angle X-ray scattering

SAXS measurements were carried out at the 12-ID-B beamline of the Advanced Photon Source (APS), Argonne National Laboratory. Crystalline NP aggregates were prepared according to a procedure described in Section 2; AB-type assemblies (rhombic dodecahedra) were prepared from a mixture of 5.28 nm Au·TMA and 5.28 nm Au·MUA; A_3B_4-type assemblies (triakis tetrahedra) were prepared from a mixture of 5.63 nm Au·TMA and 3.73 nm Au·MUA. Aqueous suspensions of NP aggregates were placed inside quartz capillaries. Each sample was exposed to X-ray beams with energy of 14 keV for 1 s. Scattered photons were counted with a Pilatus2M detector located about 2 m downstream of the sample. Collected 2D SAXS images were azimuthally averaged with the software provided at the beamline. The diffraction patterns were simulated as reported elsewhere[19,20]. For the simulation, particle sizes were determined from solution SAXS measurements. The diffraction patterns were indexed by a custom-built software and the space groups were determined to yield the highest symmetry, assuming perfect spherical particles. The Debye–Waller factor and micro-strain used for the simulation were about 2.5% and 1.0%, respectively. The domain size was approximated to about 500 nm.

The experimental and simulated data are shown in Figs. 2d and 4c of the main text.

Crystal lattice parameters derived for the AB-type structure (obtained from equally sized, 5.28 nm Au·TMA and Au·MUA): [a, b, c; α, β, γ] = [94.0 Å, 94.0 Å, 94.0 Å; 90º, 90º, 90º].
Crystal lattice parameters derived for the A_3B_4-type structure (obtained from a mixture of 5.63 nm Au·TMA and 3.73 nm Au·MUA): [a, b, c; α, β, γ] = [205.3 Å, 205.3 Å, 205.3 Å; 90º, 90º, 90º].

5. Structure determination by electron microscopy

The methodology for structure determination is based on applying a dedicated reconstruction algorithm to the aligned tilt series of 2D projection images. Owing to the relatively large size of the structures relative to the building blocks, acquisition of the tomography series was not possible for an entire assembly. Therefore, we focused on the tips of the assemblies, as illustrated in Supplementary Figs. 16 and 23. The procedure is described in detail for the AB-type assembly (Section 5.1); the same procedure was adapted for the A_3B_4 structure (Section 5.2).

5.1. AB-type assemblies

Rhombic dodecahedra were prepared from a mixture of 5.28 nm Au·TMA and 5.28 nm Au·MUA according to a procedure described in Section 2. The tilt series for electron tomography were collected from the rhombic dodecahedron shown in Supplementary Fig. 16.

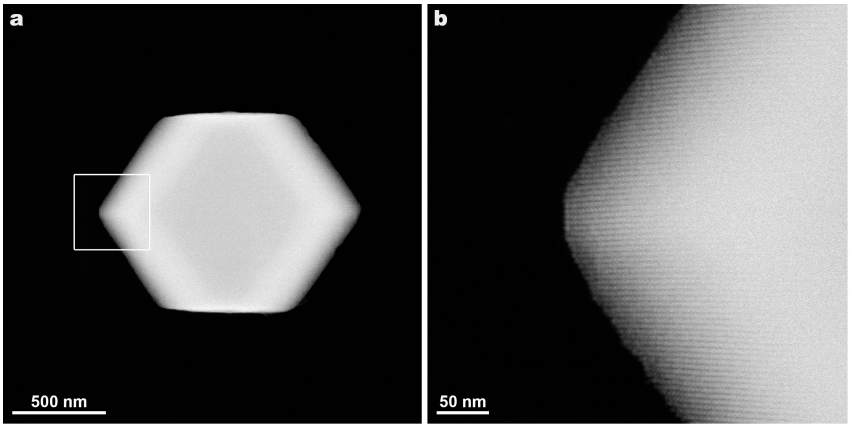

Supplementary Fig. 16 | *Left*: A high-angle annular dark-field scanning transmission electron microscopy (HAADF-STEM) image of a rhombic dodecahedron. *Right*: The tip of the rhombic dodecahedron denoted by a white frame on the left; the tip was used for acquiring electron tomography series.

Acquisition: Tilt series for electron tomography were acquired over a tilt range of –70º to +72º, with a tilt increment of 2º. We acquired five consecutive images for each tilt angle (i.e., a total of 360 images), imaging the same area of interest with a short dwell time (1s scan time per frame). In this manner, we can avoid image artefacts related to sample drift, which may otherwise occur during long acquisition times.

Alignment and reconstruction: For each frame, scanning distortions and detector noise were corrected by using a novel methodology based on deep convolutional neural networks (CNNs)[21] (Supplementary Fig. 17b). The five resulting corrected images were used as input for rigid and nonrigid registration procedures, resulting in an average image with a high signal-to-noise-ratio, as shown in Supplementary Fig. 17c. This approach was repeated for each projection of the tilt series.

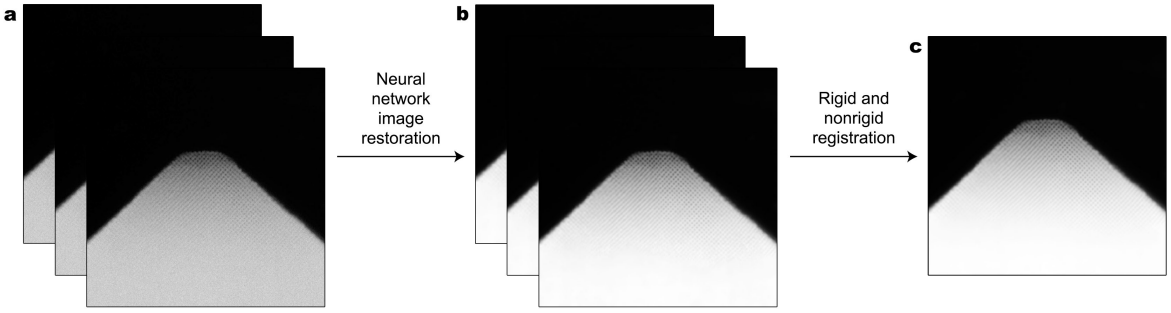

Supplementary Fig. 17 | HAADF-STEM images at 0º tilt. **a,** Raw data. **b,** Corrected data. **c,** An averaged image.

Next, the tilt series obtained in this manner were aligned using an iterative method based on phase correlation. The aligned tilt series were reconstructed using the simultaneous iterative reconstruction technique (SIRT).[22] A 3D representation of the reconstructed volume along two different viewing directions is shown in Supplementary Fig. 18.

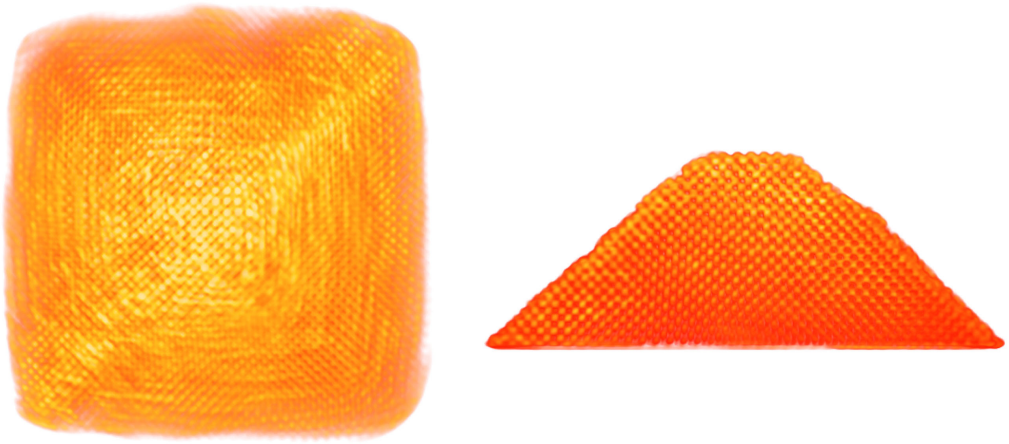

Supplementary Fig. 18 | A three-dimensional reconstructed volume for a rhombic dodecahedron (see Supplementary Fig. 16) along two different viewing directions.

To verify that the prolonged electron beam exposure required to collect data for tomography does not affect the structure of the assemblies, we imaged the same region before and after data acquisition; no appreciable differences were found (Supplementary Fig. 19).

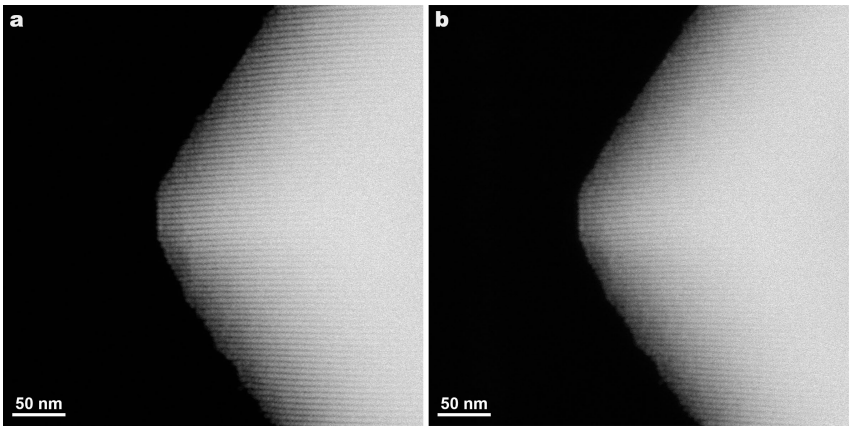

Supplementary Fig. 19 | **a,** HAADF-STEM image of a rhombic dodecahedron's tip before acquiring the tilt series. **b,** HAADF-STEM image of the same location after acquiring the tilt series.

Unit cell determination: In order to extract the lattice parameters, we first calculated a 3D Fourier transform from the reconstructed volume (Supplementary Fig. 20a). After removing the background, peak detection for the diffraction spots was performed; in order to determine the positions of the peaks with subpixel accuracy, a 3D Gaussian function was fitted to each peak. Next, we selected a set of three vectors, giving rise to a 3D grid (Supplementary Fig. 20b, *left*) that could describe the positions of all peaks in the Fourier space (Supplementary Fig. 20b, *right*). Then, an optimization procedure was performed by minimizing the sum of the Euclidean distances between the detected peaks and the points in the grid. If after optimization the grid points did not overlap with all the peaks detected in 3D, another set of three vectors was chosen.

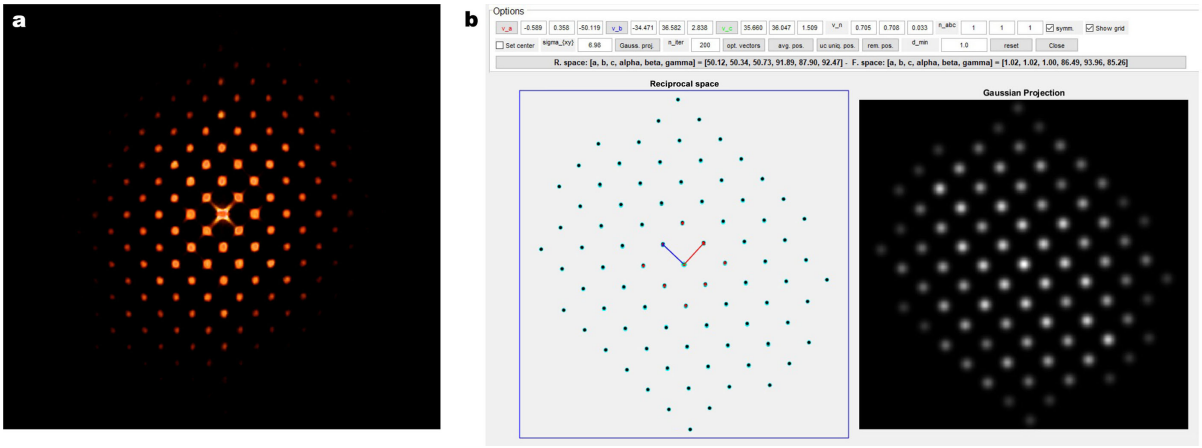

Supplementary Fig. 20 | **a,** A 3D Fourier transform pattern obtained from the reconstructed volume shown in Supplementary Fig. 18. **b,** Graphic user interface software designed to identify a set of three vectors generating a grid (left) describing the positions of all the peaks in the Fourier space (right).

From the optimized reciprocal vectors, real-space vectors were calculated and used to construct the primitive unit cell. The primitive unit cell provides information on the coordinates of the particles at the corners of the unit cell, but not of the one or more particles inside the unit cell. To determine the complete structure of the unit cell, we first overlaid the primitive unit cell with subregions of the 3D reconstruction. Once a match was found (Supplementary Fig. 21), the reconstructed volume was cropped and one or more additional building blocks (i.e., in addition to those comprising the primitive unit) were segmented (Supplementary Fig. 21, inset).

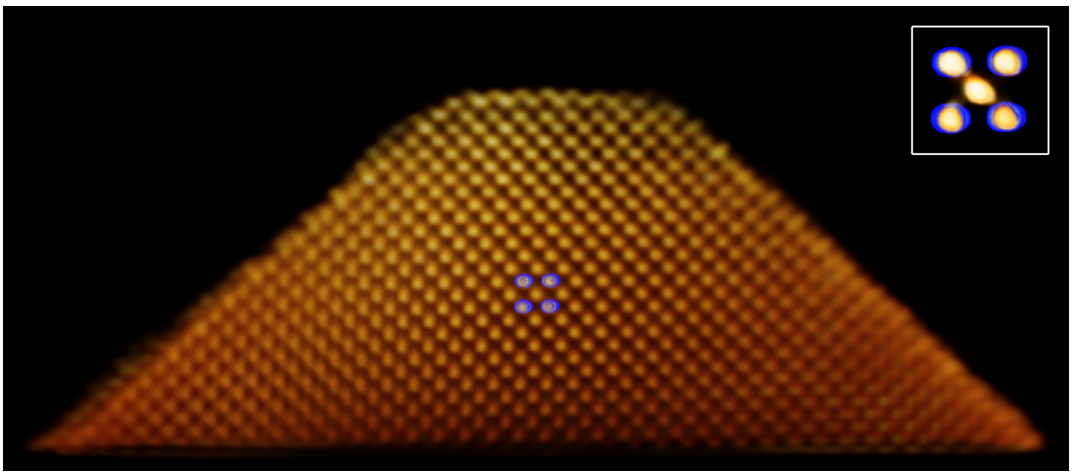

Supplementary Fig. 21 | Overlay of a primitive cell on the reconstructed volume. *Inset:* Cropped volume for a single unit cell.

Whereas the coordinates of the particles at the corners of the unit cell represent the entire 3D reconstructed volume, the position of the middle particle refers to only one particular location within the reconstructed volume. In order to determine the complete unit cell that represents a larger volume, we first replicated the obtained unit cell (Supplementary Fig. 21, inset) 3.5 times in all three dimensions (Supplementary Fig. 22a). Next, we performed an intensity fitting procedure, in which the lattice vectors and the parameters of each particle within the unit cell were optimized in order to best fit the selected part of the reconstructed volume (yellow in Supplementary Fig. 22) and the positions of the segmented particles (green in Supplementary Fig. 22). To this end, we first fitted the intensity

of the 3.5×3.5×3.5 reconstructed volume to 128 Gaussian functions. Then, we collectively optimized i) the lattice vectors, ii) the heights and sigmas of the Gaussian functions, and iii) their 3D positions (Supplementary Fig. 22b), such that the positions of all the particles within the 3.5×3.5×3.5 volume can be obtained by replicating a single unit cell in 3D. This unit cell, representing the 3.5×3.5×3.5 volume, is shown in Supplementary Fig. 22c. This unit cell is a compromise between averaging over the entire reconstructed volume (for particles comprising the primitive unit cell) and determining the coordinates of the interior particle for one specific location within the volume.

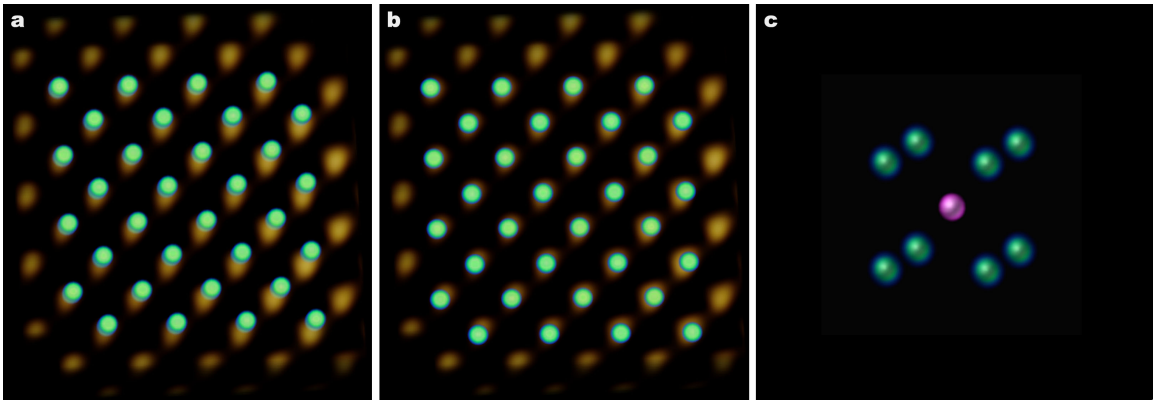

Supplementary Fig. 22 | **a,** Overlay of the segmented volume (green) on the reconstructed volume (yellow) of the AB-type assembly before optimization. **b,** Overlay of the segmented volume on the reconstructed volume after optimization. **c,** Unit cell averaged over a volume of 3.5×3.5×3.5 unit cells.

Crystal lattice parameters:
Real-space vectors before optimization, [a, b, c; α, β, γ] = [77.84 Å, 77.43 Å, 76.66 Å; 92.19º, 87.60º, 86.80º].
Real-space vectors after optimization, [a, b, c; α, β, γ] = [79.18 Å, 79.63 Å, 79.07 Å, 91.22º, 88.13º, 87.09º].

Coordinates of the building blocks:
[x y z] = [0 0 0], [0.5085 0.5052 0.5082].

The electron tomography data are publicly available at http://realnano.uantwerpen.be/demos/AB.html.

5.2. A_3B_4-type assemblies

Triakis tetrahedra were prepared from a mixture of 5.63 nm Au·TMA and 3.73 nm Au·MUA according to a procedure described in Section 2. The tilt series for electron tomography were collected on the triakis tetrahedron shown in Supplementary Fig. 23.

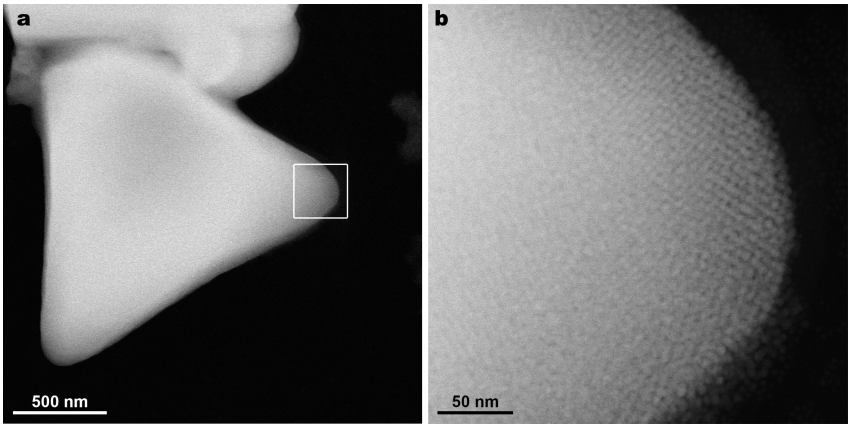

Supplementary Fig. 23 | *Left*: A HAADF-STEM image of a triakis tetrahedron. *Right*: Tip of the triakis tetrahedron denoted by a white frame on the left; the tip was used for acquiring electron tomography series.

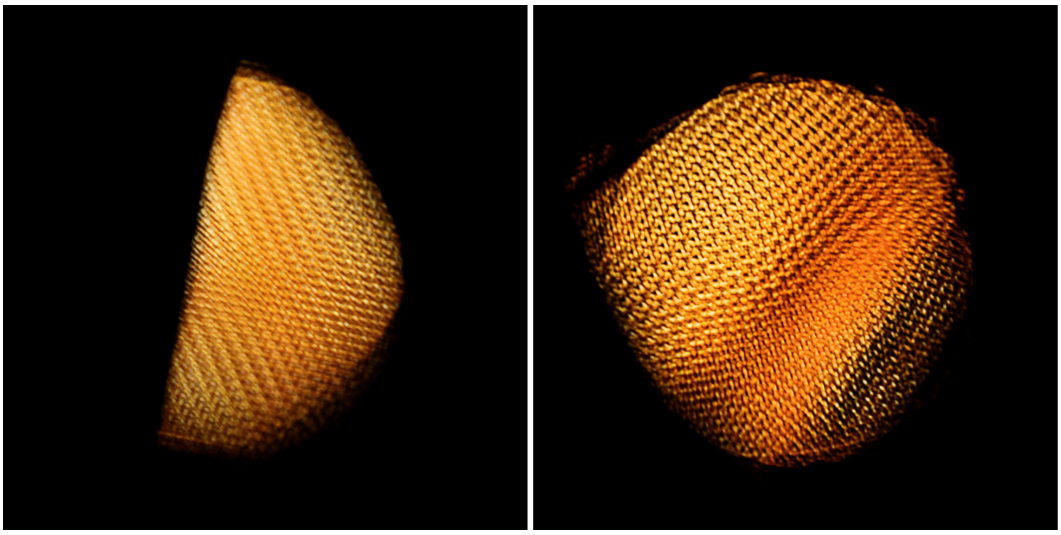

Supplementary Fig. 24 | A three-dimensional reconstructed volume for a triakis tetrahedron (see Supplementary Fig. 23) along two different viewing directions.

To verify that the prolonged electron beam exposure required to collect data for tomography does not affect the structure of the assemblies, we imaged the same region before and after data acquisition; no appreciable differences were found (Supplementary Fig. 25).

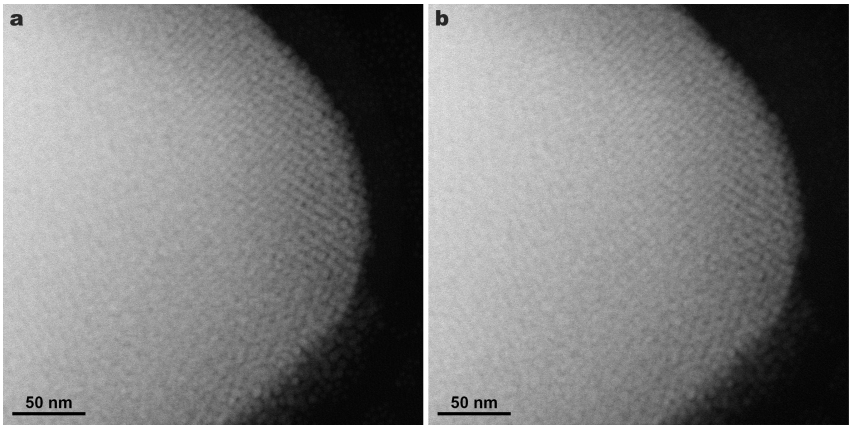

Supplementary Fig. 25 | a, HAADF-STEM image of a triakis tetrahedron's tip before acquiring the tilt series. **b,** HAADF-STEM image of the same location after acquiring the tilt series.

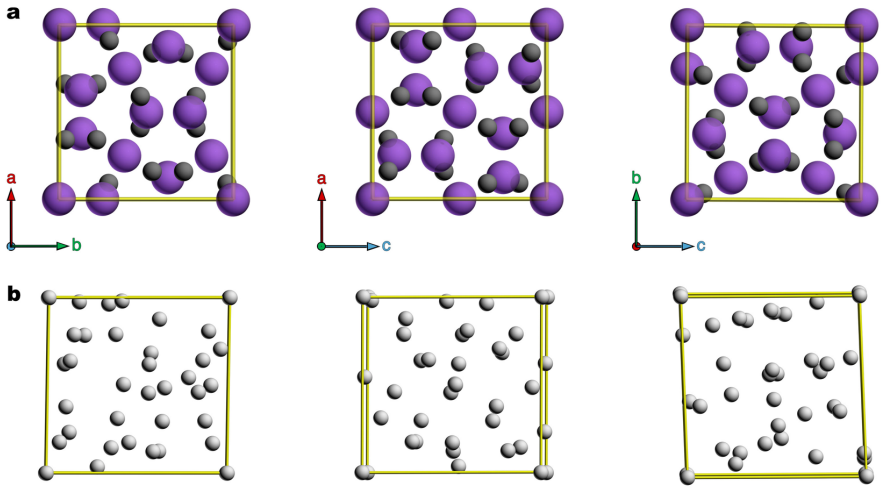

Supplementary Fig. 26 | a, Structural model of the A_3B_4-type assemblies determined by SAXS. **b,** Structural model of the A_3B_4-type assemblies determined by electron tomography.

Crystal lattice parameters:
Real-space vectors before optimization, [a, b, c; α, β, γ] = [165.26 Å, 161.00 Å, 164.31 Å; 89.80º, 91.07º, 88.94º].
Real-space vectors after optimization, [a, b, c; α, β, γ] = [166.00 Å, 160.90 Å, 164.06 Å; 89.66º, 91.82º, 89.07º].

Coordinates of the building blocks:
[x y z] = [0 0 0], [0.0456 0.2940 0.2386], [0.1133 0.1915 0.4216], [0.4297 0.3162 0.2350], [0.3506 0.5144 0.0624], [0.6255 0.2094 0.1624], [0.0966 0.5002 0.4837], [0.4393 0.3808 0.4769], [0.1436 0.3570 0.6370], [0.6677 0.0363 0.3291], [0.3611 0.7057 0.2820], [0.3869 0.1228 0.7727], [0.4408 0.5443 0.5197], [0.7990 0.2142 0.4664], [0.5795 0.4951 0.4997], [0.0818 0.8308 0.4991], [0.3785 0.8754 0.1961], [0.1267 0.7035 0.6754], [0.9066 0.3780 0.0057], [0.1662 0.5394 0.8267], [0.8313 0.0241 0.5575], [0.6412 0.8558 0.1352], [0.4104 0.8782 0.5038], [0.2219 0.4557 0.9949], [0.8952 0.6222 0.2777], [0.5964 0.0189 0.9709], [0.8744 0.7675 0.0067], [0.8769 0.3617 0.6997], [0.8575 0.2117 0.7967], [0.5456 0.8257 0.7367], [0.7168 0.9646 0.4823], [0.9296 0.8242 0.7284], [0.6116 0.6887 0.9148].

The electron tomography data are publicly available at http://realnano.uantwerpen.be/demos/A3B4.html.

6. Modeling of crystalline aggregates from charged nanoparticles

6.1. Geometric criteria for the formation of the AB and A_3B_4 lattices

The AB lattice

Based solely on the geometric criterion, one can assume that the AB (CsCl-type) lattice from oppositely charged NPs can form if the NP size ratio and the lattice constant allow oppositely charged NPs to be in direct contact. For a given lattice constant d (see Supplementary Fig. 27a), the distances between the centers of two particles A and between the centers of A and B are equal to d and to half the cube body diagonal, $\frac{\sqrt{3}}{2}d$, respectively. Let us consider the case when we vary the ratio of the sizes of particles A and B, d_A/d_B, where particles A are larger than particles B. The AB lattice will be stable and exist only when and the particles A and B are in direct contact; when particles B are so small that they cannot remain in direct contact with particles A, whereas particles A are in direct contact (i.e., repulsion), the AB lattice should be unstable. These geometric arguments show that the AB lattice should fail to form when d_A/d_B is greater than ~1.366.

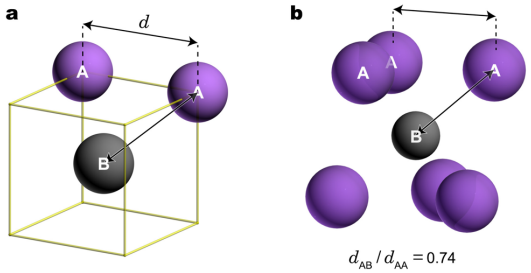

Supplementary Fig. 27 | **a,** Schematic representation of the AB (CsCl-type) lattice. **b,** Schematic representation of the A_3B_4 (Th_3P_4-type) lattice.

The A_3B_4 lattice

Following the same arguments, the A_3B_4 lattice should form if the size ratio of particles A and B and the lattice constant allow the oppositely charged particles in the unit cell to be in direct contact; otherwise, the lattice should be unstable. A schematic representation of the A_3B_4 lattice is shown in Supplementary Fig. 27b; the lattice will fail to form for $d_A/d_B > \frac{d_{AA}}{2d_{AB}-d_{AA}}$, which can be expressed as a function of d_{AB}/d_{AA} as $\frac{d_A}{d_B} > \frac{1}{2d_{AB}/d_{AA}-1}$. With the interatomic distances from the structure of Th_3P_4 (d_{Th-Th} = 4.0363 Å and d_{Th-P} = 2.9869 Å), d_{AB}/d_{AA} = 0.74 and $d_A/d_B > 2.083$.

The results of the above geometric considerations have been overlaid on the phase diagram of the experimentally found lattices and a rough agreement between these two has been found (Supplementary Fig. 28).

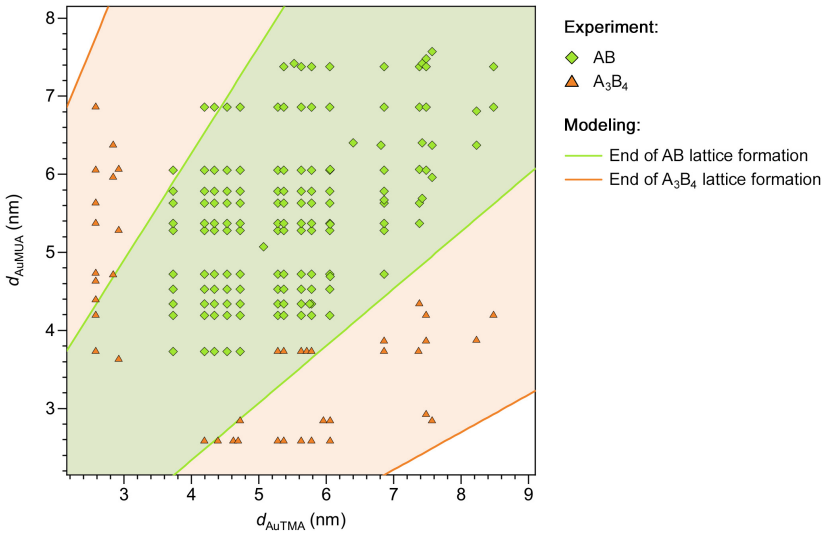

Supplementary Fig. 28 | Phase diagram of the experimentally observed lattices (markers) and the boundaries of existence of the two types of lattices predicted based on the geometric criterion (lines).

6.2. A numerical model of lattice formation based on the free-energy profiles

We also developed a hybrid modeling approach combining classical atomistic MD simulations with analytical modeling to establish principles governing the self-assembly of charged nanoparticles in electrolyte solutions. In this approach, first, we determined the Gibbs free-energies of attractive and repulsive coupling of pairs of NPs used in the experiments, as described above (Section 3; the simulations were performed in a $(NH_4)_2CO_3$ solution at a concentration (4.28 M) matching that corresponding to the onset of NP self-assembly in a typical experiment). Then, we used the obtained free-energy profiles (Fig. 1e in the main text) to calculate the lattice free-energies for the experimentally observed AB-type and A_3B_4-type superlattices. The resulting lattice free-energies were used to construct phase diagrams (Supplementary Fig. 29), which were compared with the experimental results (Fig. 1c).

More specifically, the lattice free-energies (per elementary cell) were calculated by counting the number of first-neighbor, second-neighbor, and, in some cases, third-neighbor contacts between NPs within the elementary cells in the AB and A_3B_4 lattices, and summing over the NP–NP interaction free-energies (Fig. 1e), calculated for distances resulting from these contacts. The lattice free-energies were evaluated for all the possible combinations of NP sizes in the range 2.3–9.5 nm. For the selected NP sizes and the chosen lattice type, our code found the optimal lattice constants, which resulted in the smallest lattice free-energies.

The lattice free-energies, considering only the attractive and repulsive interactions between the first few NP neighbors, can be defined as:

- For the AB-type lattice: $E_{latt} = 8 \cdot E_{AB} \cdot s_{AB} + 3 \cdot E_{AA} \cdot s_{AA} + 3 \cdot E_{BB} \cdot s_{BB}$,

where E_{AB}, E_{AA}, and E_{BB} are pairwise interaction free-energies for the A–B (attractive), A–A, and B–B (both repulsive) particle pairs, and s_{AB}, s_{AA}, and s_{BB} are scaling factors (discussed below). For the selected NP sizes and the AB lattice constant, our code determined the NP–NP distances, free energies of pairwise interactions (according to the free-energy profiles in Fig. 1e), and the lattice free-energies. Based on these results, the lowest lattice free-energies (for the given NP sizes) were obtained by optimizing the lattice constants, which are plotted in Supplementary Fig. 29a.

- For for A_3B_4-type lattice: $E_{latt} = (12 \cdot E_{AB1} + 12 \cdot E_{AB2}) \cdot s_{AB} + 6 \cdot E_{AA1} \cdot s_{AA} + (6 \cdot E_{BB1} + 4 \cdot E_{BB2} + 6 \cdot E_{BB3}) \cdot s_{BB}$,

where E_{ABi}, E_{AAi}, and E_{BBi} (i = interaction index) are pairwise interaction free-energies for the A–B, A–A, and B–B particle pairs and s_{AB}, s_{AA}, and s_{BB} are the scaling factors. Considering that the A_3B_4 lattice has a unit length of 10, the selected interparticle distances are 2.954 for E_{AB1}, 3.031 for E_{AB2}, 4.044 for E_{AA1}, 3.3256 for E_{BB1}, 3.744 for E_{BB2}, and 4.216 for E_{BB3}. The lowest lattice free-energies are calculated as above for the optimal lattice constants and they are plotted in Supplementary Fig. 29b. Owing to the presence of three large and four small NPs in the elementary unit cell of the A_3B_4 lattice, the plotted E_{latt} was divided by 3 – i.e., the total lattice energies for all three lattices have been normalized by the number of the large (A) NPs in their elementary unit cells (1 for AB and 3 for A_3B_4).

Scaling factors: As the starting point for calculating the lattice free-energies, we used the free-energy profiles shown in Fig. 1e (the main text). However, these energy profiles were obtained for NPs with an inorganic core of 5 nm. In order to evaluate the interaction energies (E_{AB}, E_{AA}, E_{BB}, etc.) of NPs with core sizes that differ from 5 nm, the energies of the interparticle interactions were scaled up or down. The scaling was performed by multiplying the pairwise free-energy terms, E_{AB}, E_{AA}, E_{BB} (and other analogous terms when multiple types of A–B, A–A, and B–B interactions are present in the above formulas for lattice energies), by factors of $d_A d_B/d_0^2$, $d_A d_A/d_0^2$, and $d_B d_B/d_0^2$, where d_0 = 5 nm, and d_A and d_B denote the diameters of NPs A and B.

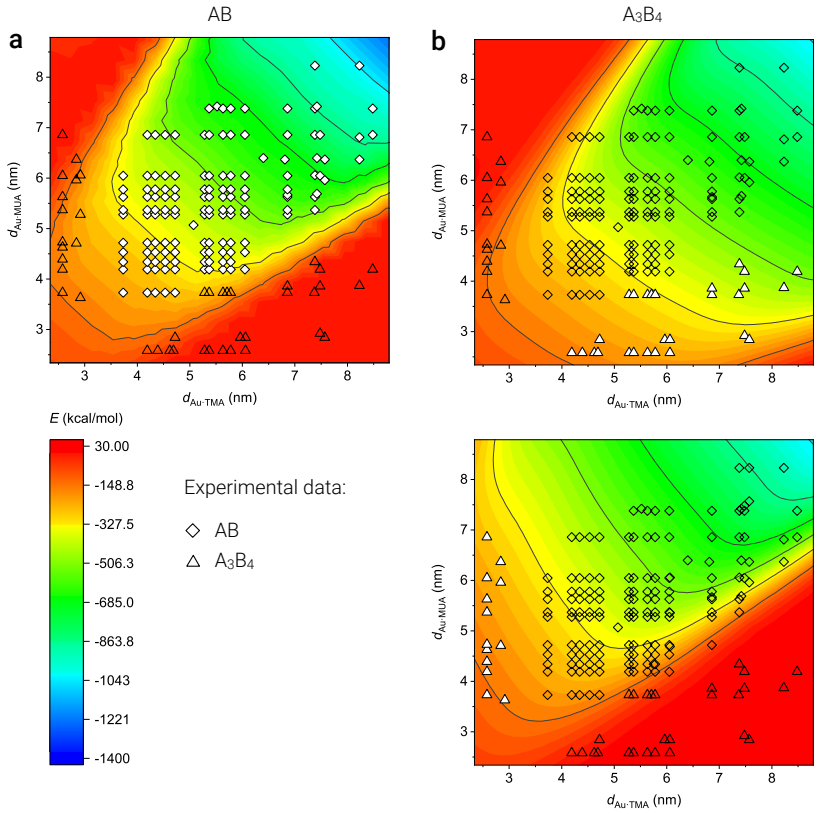

Supplementary Fig. 29 | The lowest lattice free-energies for **a,** the AB lattice and **b,** the A_3B_4 lattice as a function of NP core size. The lattice energy contour maps are overlaid with data points determined experimentally. Within the A_3B_4 lattice, Au·TMA NPs can reside in positions A or B (the top and the bottom panel of **b**, respectively). The data presented here were used to highlight regions with significantly low free-energy minima on the phase diagram of the experimentally observed lattices (Fig. 1c in the main text) (we note that the free energies of the different lattices cannot be compared directly because of the different stoichiometries and the numbers of NPs in their unit cells; therefore, the lattice energies were formalized according to the number of large NPs).

7. Gel electrophoresis of superionic nanoparticles

Agarose gel (0.5% *w*/*w*) (Agarose I™, VWR Life Science) was immersed in a 0.5 M $NaHCO_3/Na_2CO_3$ buffer (pH = 9.4). The gel was run in a horizontal electrophoresis system (Mini-Sub Cell GT Systems, Bio-Rad Laboratories). Solutions of 4.83 nm Au·TMA and 4.83 nm Au·MUA (c = 2 mg/mL) in water were prepared, the solutions were saturated with $(NH_4)_2CO_3$ by adding an excess (1.1 g per 1 mL) of solid $(NH_4)_2CO_3$; 15 µL of the resulting solutions were withdrawn from above undissolved $(NH_4)_2CO_3$ and applied into wells **a** and **d**, respectively. For well **c**, Au·TMA and Au·MUA (c = 2 mg/mL each) were mixed in a 1:1 ratio, resulting in a black precipitate; the mixture was heated at 70 ºC for 24 h (to mimic the conditions used previously for the self-assembly of ionic NPs), resulting in ligand equilibration to afford a single species Au·(TMA/MUA) well-soluble in water. The resulting solution was saturated with $(NH_4)_2CO_3$ as above and 15 µL were applied into the well. For well **b**, Au·TMA and Au·MUA were mixed in a 1:1 ratio; the resulting aggregate was collected by centrifugation and suspended in pure water, which was then saturated with $(NH_4)_2CO_3$ as above, resulting in the disassembly of the Au·TMA/Au·MUA aggregate (the final concentrations, $c_{Au\cdot TMA} = c_{Au\cdot MUA}$ = 2 mg/mL) (here, we mimic the conditions used for the self-assembly of ionic NPs in the current study). 15 µL of the resulting solution was applied into the well. The electrophoresis was run at a current of 2,000 mA for 3 min, followed by at 1,000 mA for 30 min (PowerPac Universal Power Supply, Bio-Rad Laboratories).

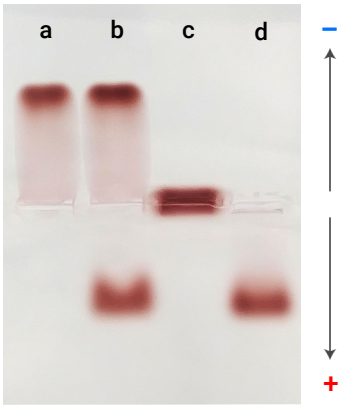

Supplementary Fig. 30 | Gel electrophoresis of superionic nanoparticles. Lane **a**: 4.83 nm Au·TMA; Lane **b**: a 1:1 mixture of 4.83 nm Au·TMA and 4.83 nm Au·MUA; Lane **c**: 4.83 nm Au·(TMA/MUA); Lane **d**: 4.83 nm Au·MUA.

Effect of nanoparticle preheating on self-assembly behavior: To confirm that the previously reported coassemblies of oppositely charged NPs are made of NPs that underwent a significant extent of ligand mixing, we subjected our superionic building blocks—Au·TMA and Au·MUA—to conditions described by i) Grzybowski *et al.*[23] and ii) Pileni *et al.*[24] To this end, i) we titrated Au·TMA with equally sized Au·MUA in water, resulting in the precipitation of an amorphous aggregate. The aggregate was dissolved upon heating in water at 60 ºC (complete dissolution was observed after 40 h). Then, 1 volume of DMSO was added and heating was continued at 50 ºC, leading to a gradual decrease in the volume fraction of water. After 18.5 h, the solution turned colorless and the precipitate was inspected by SEM, revealing the presence of colloidal crystals having morphologies typical of the ZnS-type structure (Supplementary Fig. 31, bottom left), as reported before.[23] At a near-zero ionic strength and in the presence of DMSO (having a dielectric constant lower than that of water), self-assembly is governed predominantly by long-range electrostatic interactions, which explains the formation of non-closed-packed crystals with a ZnS-like structure even from NPs having a small excess of one ligand over the other.

In the second set of experiments, we first coassembled Au·TMA and Au·MUA into CsCl-type crystals according to our procedure (Section 2). Then, we heated the resulting crystalline precipitate in water at 70 ºC for 24 h to allow for an exhaustive ligand exchange (which resulted in a solution of colloidally stable NPs). This procedure equalized the numbers of TMA and MUA ligands on both types of NPs, resulting in essentially a single NP type, which we denote as Au·(TMA/MUA) (see Supplementary Fig. 31c). Then, 1 volume of DMSO was added and the fraction of water was decreased by heating at 40 ºC. This process was discontinued after 60 h, when the NPs precipitated and the solution turned colorless. Inspection of the black solid by SEM revealed the presence of colloidal crystals with habits typical of the face-centered cubic (*fcc*) phase, as described before[24] (we note that our assemblies are slightly different from those reported before because our Au·TMA NPs contain a small fraction of hexanethiol as the background ligand; see Section 1.2 above).

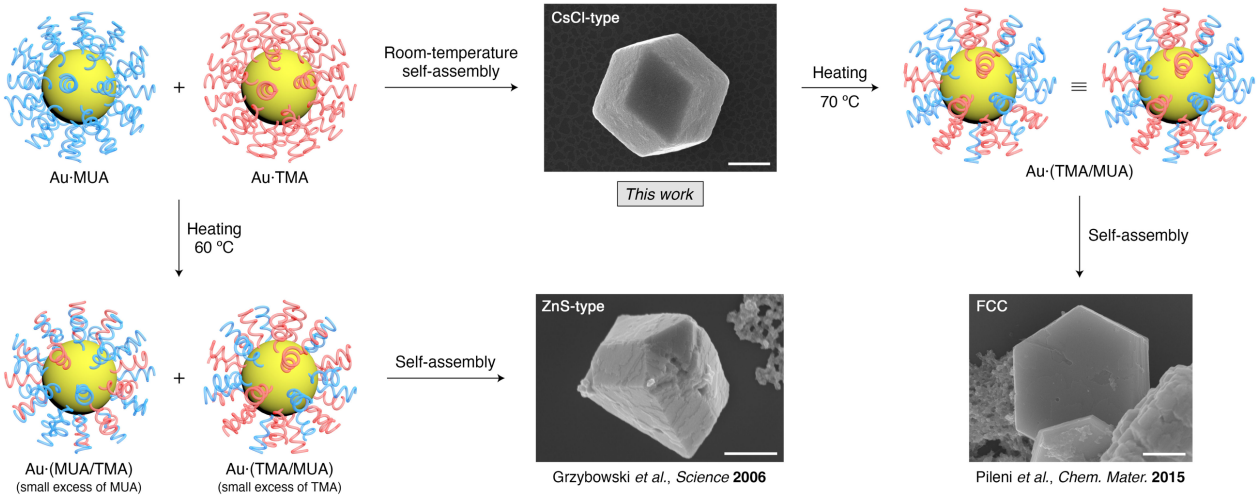

Supplementary Fig. 31 | Control experiments with charged NPs subjected to heating in the presence of oppositely charged NPs prior to self-assembly. Scale bars = 500 nm.

8. Supplementary references

1. Peng, S. et al. A facile synthesis of monodisperse Au nanoparticles and their catalysis of CO oxidation. *Nano Res.* **1**, 229–234 (2008).
2. Ho, S. F. et al. A facile route to monodisperse MPd (M = Co or Cu) alloy nanoparticles and their catalysis for electrooxidation of formic acid. *Nanoscale* **6**, 6970–6973 (2014).
3. Leff, D. V., Ohara, P. C., Heath, J. R. & Gelbart, W. M. Thermodynamic control of gold nanocrystal size: Experiment and theory. *J. Phys. Chem.* **99**, 7036–7041 (1995).
4. Jong, L. I. & Abbott, N. L. Rate-dependent lowering of surface tension during transformations of water-soluble surfactants from bolaform to monomeric structures. *Langmuir* **14**, 2235–2237 (1998).
5. Chu, Z., Han, Y., Král, P. & Klajn, R. "Precipitation on nanoparticles": Attractive intermolecular interactions stabilize specific ligand ratios on the surfaces of nanoparticles. *Angew. Chem. Int. Ed.* **57**, 7023–7027 (2018).
6. Chu, Z. et al. Supramolecular control of azobenzene switching on nanoparticles. *J. Am. Chem. Soc.* **141**, 1949–1960 (2019).
7. Si, K. J., Chen, Y., Shi, Q. & Cheng, W. Nanoparticle superlattices: The roles of soft ligands. *Adv. Sci.* **5**, 1700179 (2018).
8. He, J. et al. Diffusion and filtration properties of self-assembled gold nanocrystal membranes. *Nano Lett.* **11**, 2430–2435 (2011).

9. Bera, M. K. et al. Interfacial localization and voltage-tunable arrays of charged nanoparticles. *Nano Lett.* **14**, 6816–6822 (2014).
10. Zhao, H. et al. Reversible trapping and reaction acceleration within dynamically self-assembling nanoflasks. *Nat. Nanotechnol.* **11**, 82–88 (2016).
11. Humphrey, W., Dalke, A. & Schulten, K. VMD: Visual molecular dynamics. *J. Mol. Graph.* **14**, 33–38 (1996).
12. Grossfield, A. WHAM: The weighted histogram analysis method; University of Rochester Medical Center; Rochester, NY (2012; accessed April 2017).
13. Kumar, S., Bouzida, D., Swendsen, R. H., Kollman, P. A. & Rosenberg, J. M. The weighted histogram analysis method for free-energy calculations on biomolecules. I. The method. *J. Comput. Chem.* **13**, 1011–1021 (1992).
14. Phillips, J. C. et al. Scalable molecular dynamics with NAMD. *J. Comput. Chem.* **26**, 1781–1802 (2005).
15. Vanommeslaeghe, K. et al. CHARMM general force field: A force field for drug-like molecules compatible with the CHARMM all-atom additive biological force fields. *J. Comput. Chem.* **31**, 671–690 (2010).
16. Yu, W., He, X., Vanommeslaeghe, K. & MacKerell, A. D., Jr. Extension of the CHARMM general force field to sulfonyl-containing compounds and its utility in biomolecular simulations. *J. Comput. Chem.* **33**, 2451–2468 (2012).
17. Vanommeslaeghe, K. & MacKerell, A. D., Jr. Automation of the CHARMM general force field (CGenFF) I: Bond perception and atom typing. *J. Chem. Inf. Model.* **52**, 3144–3154 (2012).
18. Darden, T., York, D. & Pedersen, L. Particle mesh Ewald: An $N\cdot\log(N)$ method for Ewald sums in large systems. *J. Chem. Phys.* **98**, 10089 (1993).
19. Senesi, A. J. & Lee, B. Small-angle scattering of particle assemblies. *J. Appl. Crystallogr.* **48**, 1172–1182 (2015).
20. Macfarlane, R. J. et al. Nanoparticle superlattice engineering with DNA. *Science* **334**, 204–208 (2011).
21. Altantzis, T. et al. Three-dimensional quantification of the facet evolution of Pt nanoparticles in a variable gaseous environment. *Nano Lett.* **19**, 477–481 (2019).
22. Gilbert, P. Iterative methods for the three-dimensional reconstruction of an object from projections. *J. Theor. Biol.* **36**, 105–117 (1972).
23. Kalsin, A. M. et al. Electrostatic self-assembly of binary nanoparticle crystals with a diamond-like lattice. *Science* **312**, 420–424 (2006)
24. Wang, L., Albouy, P.-A. & Pileni, M.-P. Synthesis and self-assembly behavior of charged Au nanocrystals in aqueous solution. *Chem. Mater.* **27**, 4431–4440 (2015).